

STRUCTURAL BIOLOGY

Multistate kinetics of the syringe-like injection mechanism of Tc toxins

Peter Njenga Ng'ang'a^{1†}, Julian Folz^{2†}, Svetlana Kucher^{3,4†}, Daniel Roderer^{1†‡}, Ying Xu^{5,6}, Oleg Sitsel^{1§}, Alexander Belyy^{1¶}, Daniel Prumbaum¹, Ralf Kühnemuth², Tufa E. Assafa⁴, Min Dong^{5,6}, Claus A. M. Seidel^{2*}, Enrica Bordignon^{3,4*}, Stefan Raunser^{1*}

Tc toxins are pore-forming virulence factors of many pathogenic bacteria. Following pH-induced conformational changes, they perforate the target membrane like a syringe to translocate toxic enzymes into a cell. Although this complex transformation has been structurally well studied, the reaction pathway and the resulting temporal evolution have remained elusive. We used an integrated biophysical approach to monitor prepore-to-pore transition and found a reaction time of ~30 hours for a complete transition. We show two asynchronous general steps of the process, shell opening and channel ejection, with the overall reaction pathway being a slow multistep process involving three intermediates. Liposomes, an increasingly high pH, or receptors facilitate shell opening, which is directly correlated with an increased rate of the prepore-to-pore transition. Channel ejection is a near-instantaneous process which occurs with a transition time of <60 milliseconds. Understanding the mechanism of action of Tc toxins and unveiling modulators of the kinetics are key steps toward their application as biomedical devices or biopesticides.

INTRODUCTION

Toxin complexes (Tc) are pathogenicity factors in various bacteria that infect insects or mammals (1–3). While Tcs from insect pathogenic bacteria, such as *Photorhabdus luminescens* (4) or *Xenorhabdus nematophila* (5), show potential for biotechnological applications (6), Tcs of human pathogenic bacteria such as *Yersinia pseudotuberculosis* (7) or *Yersinia enterocolitica* (8) may also play an important role in infectious diseases.

Tc toxins use a special syringe-like mechanism to perforate the host cell membrane and inject a deadly enzyme into the host cytosol. They are composed of three components: TcA, TcB, and TcC (9, 10). TcA is the key component for receptor binding, pore formation, and translocation of the toxin (11, 12). It forms a bell-shaped homopentamer of ~1.4 to 1.7 MDa made up of a central, α -helical channel surrounded by a shell, to which it is connected by a stretched linker (13). The receptor-binding domains (RBDs) at the surface of the shell are structurally variable (14), allowing the association of various Tc toxins to different receptors, such as glycans (12, 15–17) or highly glycosylated protein receptors such as Visgun (Vsg) (18).

TcB and TcC together form a hollow cocoon of ~250 kDa that encapsulates the ~30-kDa C-terminal domain of TcC (19, 20), also

known as the hypervariable region (HVR). The HVR is the actual toxic enzyme that is autoproteolytically cleaved inside the cocoon (19, 20). In the case of TccC3 from *P. luminescens*, the HVR is an adenosine diphosphate ribosyltransferase, which modifies F-actin at threonine-148 (21–23) leading to disorganization of the target cell's cytoskeleton. The TcA pentamer and TcB-TcC heterodimer spontaneously assemble with subnanomolar affinity to form the ~1.7-MDa ABC holotoxin (24).

In the prepore form of the holotoxin, the shell of TcA is closed. A pH change to either acidic (23) or basic (11, 25) conditions results in the opening of the shell. Subsequently, the stretched linkers between the shell and the channel condense rubber band-like from an extended, unfolded conformation to a compact, partially folded conformation. As a consequence, the channel is ejected and enters the target cell membrane similar to a syringe. The hydrophobic environment of the membrane triggers the opening of the tip of the channel. In this so-called pore state, the HVR is translocated through the channel into the target cell (11).

The architectures of the prepore and the pore states of Tc toxins have been well examined, elucidating the starting and end points of the transition from prepore to pore in molecular detail (24, 26). However, functional aspects of this large-scale rearrangement of the pentamer, such as the reaction pathway and its energy landscape with possible intermediate states, synchronization of the protomers, and the resulting temporal evolution are still unknown. Here, we combine electron paramagnetic resonance (EPR) spectroscopy, confocal and total internal reflection single-molecule fluorescence spectroscopy, single-particle cryo-electron microscopy (cryo-EM), and biochemistry to address these questions. We examine the Tc toxin from the *P. luminescens* strain W14, comprising TcA (TcdA1), TcB (TcdB2), and TcC (TccC3) and demonstrate that the prepore-to-pore transition of this Tc toxin at high pH has a slow reaction time of ~30 hours in vitro and involves one transient and two stable intermediate states, one in which the RBDs of the shell rearrange and a second in which the shell opens. Using single-molecule spectroscopy, we demonstrate that the slow kinetics in the ensemble arise from the low probability of initiating the otherwise fast individual channel ejection events,

Copyright © 2025 The Authors, some rights reserved; exclusive licensee American Association for the Advancement of Science. No claim to original U.S. Government Works. Distributed under a Creative Commons Attribution NonCommercial License 4.0 (CC BY-NC).

¹Department of Structural Biochemistry, Max Planck Institute of Molecular Physiology, Otto-Hahn-Str. 11, 44227 Dortmund, Germany. ²Chair of Molecular Physical Chemistry, Heinrich-Heine University Düsseldorf, Universitätsstr. 1, 40225 Düsseldorf, Germany. ³Department of Physical Chemistry, University of Geneva, Quai Ernest Ansermet 30, 1211 Geneva, Switzerland. ⁴Faculty of Chemistry and Biochemistry, Ruhr University Bochum, Universitätsstr. 150, 44801 Bochum, Germany. ⁵Department of Urology, Boston Children's Hospital, Boston, MA, USA. ⁶Department of Surgery and Department of Microbiology, Harvard Medical School, Boston, MA, USA.

*Corresponding author. Email: stefan.raunser@mpi-dortmund.mpg.de (S.R.); enrica.bordignon@unige.ch (E.B.); cseidel@hhu.de (C.A.M.S.)

†These authors contributed equally to this work.

‡Present address: Leibniz-Forschungsinstitut für Molekulare Pharmakologie, Robert-Roessle-Str. 10, 13125 Berlin, Germany.

§Present address: Marine Structural Biology Unit, Okinawa Institute of Science and Technology Graduate University, Onna, Okinawa 904-0495, Japan.

¶Present address: Membrane Enzymology Group, Groningen Institute of Biomolecular Sciences and Biotechnology, Faculty of Science and Engineering, University of Groningen, Nijenborgh 3, 9747 AG Groningen, Netherlands.

which proceed within several milliseconds. The presence of liposomes, an increasingly high pH or a receptor, such as heparin or Vsg, increases the probability of initiating the opening of the shell, an effect which can also be mimicked by biotinylation or site-directed mutagenesis, indicating that destabilization of the shell is essential for the quick transition from prepore to pore. Our results are a key contribution to a holistic understanding of the complex mechanism of action of molecular machines, particularly Tc toxins, and provide an important basis for their adaptation to biotechnological applications.

RESULTS

Receptor binding accelerates pH-dependent shell opening

We and others have previously shown that TcA binds to target cells via glycans or glycosylated surface receptors and transitions from prepore to pore, before delivering its toxic payload into the cytoplasm (11, 12, 15, 17, 18, 27). During prepore-to-pore transition, TcA undergoes two major conformational changes: shell opening and channel ejection (Fig. 1). However, there are no intermediate states known that explain whether these steps proceed simultaneously or sequentially, and no data are available on the kinetics of the reaction. We therefore set out to address the individual reaction kinetics of shell opening and channel ejection by EPR spectroscopy. In this regard, we designed TcA variants with the single-point mutation D1193C and the double-point mutation Q914C-S2365C that allows 3-(2-iodoacetamido)-proxyl (IAP) labeling to measure the changes in dynamics and interspin distances during shell opening and channel ejection in a time-resolved manner (fig. S1, A to D). Both IAP-labeled toxins were still active against human embryonic kidney (HEK) 293T cells (fig. S1, E and F), showing that site-directed mutagenesis and labeling did not interfere with holotoxin assembly, cell binding, prepore-to-pore transition, and toxin translocation.

We first focused on the opening of the shell using TcA (1193-IAP). We induced the prepore-to-pore transition by a pH shift to 11.2 and monitored the kinetics of the conformational changes via continuous wave (CW) EPR at room temperature (Fig. 2 and figs. S2 and S4) and the associated changes in the interprotomer distances via double electron-electron resonance (DEER) measurements on samples snap frozen after defined incubation times (Figs. 2C and 4A and figs. S2 and S3). Figure 2A shows schematically how we used CW EPR to extract conformational kinetics when the prepore and pore states of the toxin have different rotational dynamics at the spin-labeled site. As an example, we simulated two EPR spectra with

3-ns (slower) and 1.5-ns (faster) rotational correlation times in the two states, to demonstrate that faster motions are encoded in narrower spectral lines with increased signal intensity. The change in the spectral intensity plotted versus time allowed us to monitor the kinetics of the toxin's conformational changes (Fig. 2B). The increase of the pH to pH 11.2 revealed a spectral change from slower to faster motions in spin-labeled TcA (1193-IAP) (fig. S2A). The corresponding experimental EPR kinetics are shown in Fig. 2C (right, dots, three repeats). In addition, upon incubation at pH 11.2, short distances in DEER measurements correlated with the prepore state (figs. S1 and S3A) disappeared over time (fig. S3B), indicating the opening of the shell. The extracted DEER kinetics, representing the decrease in the population of prepore states, are shown in Fig. 2C (green triangles, extracted from fig. S3B). Together, time-resolved CW EPR kinetics and DEER revealed that the increasing dynamics of the label correlate with shell opening and proceed as a first-order reaction with a reaction time of 11 ± 1.5 hours (Fig. 2C). EPR confirmed the absence of shell opening at acidic pH in vitro (figs. S2A and S3A). Going from pH 11 to pH 11.8 accelerates the kinetics of shell opening by an order of magnitude (fig. S2, B and C).

Expectedly, holotoxin assembly, that is the binding of the TcB-TcC cocoon onto the TcA pentamer, had no major influence on the transition kinetics (fig. S2, C and F). In contrast, the shell opening was accelerated by an order of magnitude when liposomes were added instead of detergents (fig. S2, D to F), indicating that the interaction of the toxin with lipids destabilizes the shell and accelerates its opening. A similar acceleration through interaction of Tc toxins with the host membrane in vivo is therefore conceivable.

Tc toxins can potentially penetrate host cell membranes in the mid-gut directly, where shell opening is probably triggered by the high pH in this part of the insect digestive tract (28). However, the more common route of Tc toxin intoxication is via the endosomal pathway, where pore formation happens after acidification of the late endosome (29). So far, we could only reproduce the former in vitro, whereas the latter seems to depend on additional factors, such as binding to receptors. To find out whether binding of heparin, Lewis X glycans, or Vsg, which are known receptors of TcdA1 from *P. luminescens* (12, 15, 17, 18), has an influence on the pH dependence of shell opening, we incubated ABC holotoxins with the receptors at either pH 4 or pH 11.2 and monitored pore formation by negative stain EM (Fig. 3, A and B, and fig. S4, A to G). At pH 4, none of the receptors showed an effect compared to the control (fig. S4, C, E, and G). At pH 11.2, Lewis X had no effect (Fig. 3B and fig.

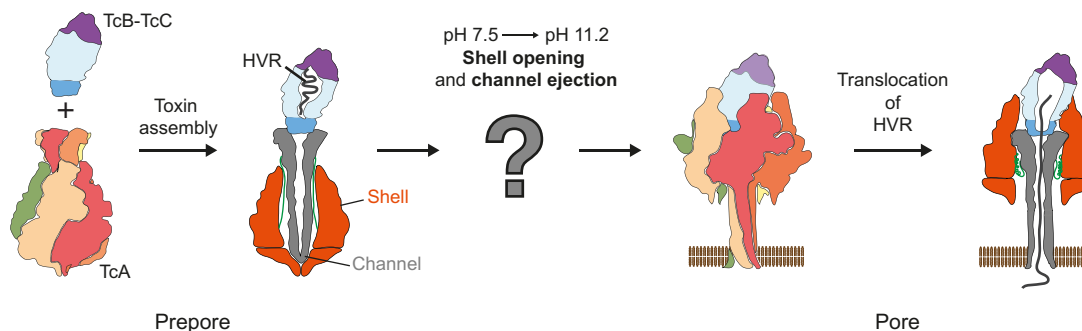


Fig. 1. Schematic overview of the functional mechanism of action of Tc toxins. The two toxin states, prepore and pore, are displayed each in two ways: as surface cartoon representations (left) and vertical cut-throughs (right). In the surface cartoon representation, the five protomers of TcA are colored differently, the TcC is violet, and TcB is in light and dark cyan. In the cut-through, TcA is orange and grey, and the HVR is highlighted in black.

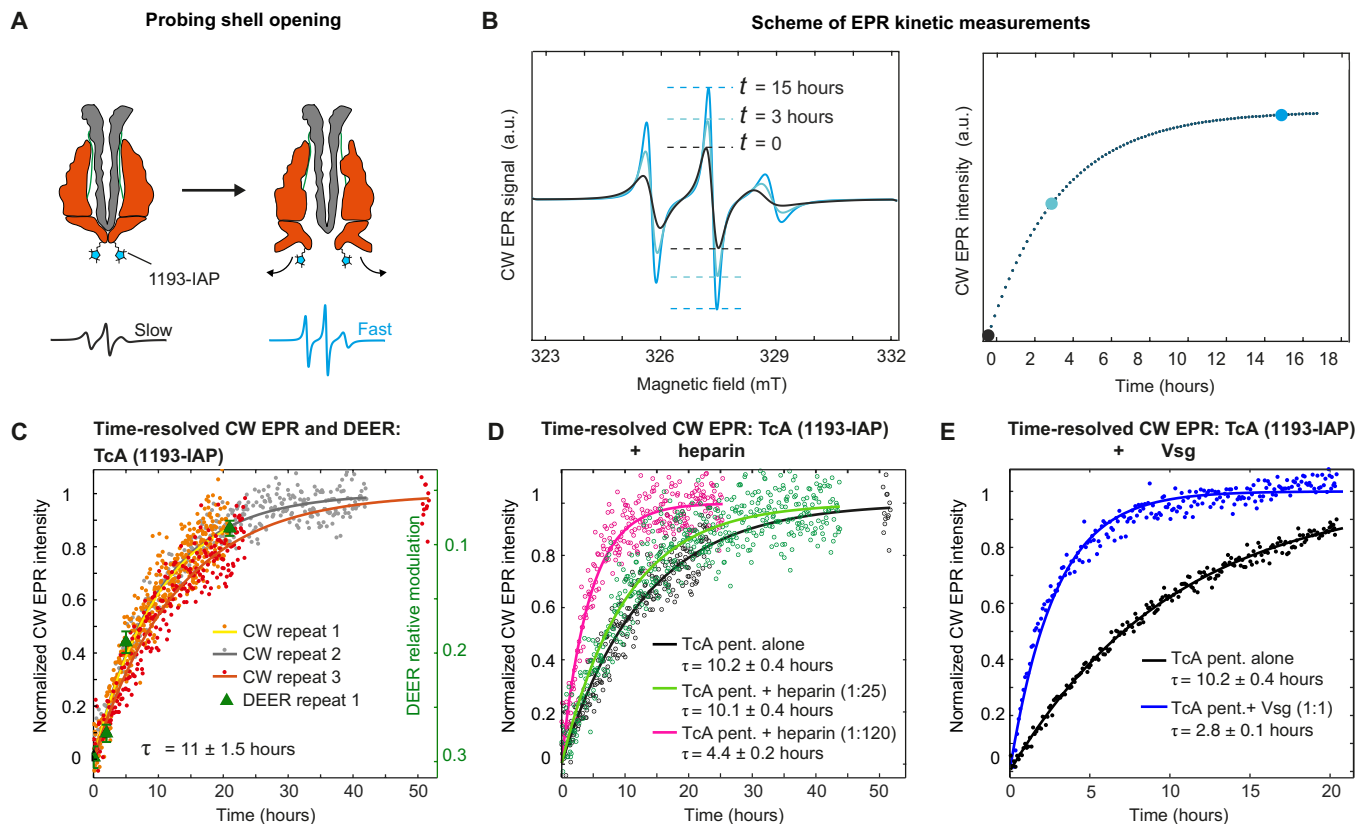


Fig. 2. EPR kinetics of TcA shell opening in the absence and presence of receptors. (A) TcA variant (1193Cys) to probe shell opening via EPR labeled with IAP, resulting in TcA (1193-IAP). Two sketches of the different CW EPR spectra of the prepore (slower motion, 3-ns rotational correlation time) and the pore (faster motion, 1.5 ns) states simulated with EasySpin (34). (B) Three simulated spectra with the slow component interconverting in 15 hours to the fast component. The kinetics of the shell opening are obtained by plotting the peak-to-peak intensity versus time (right). a.u., arbitrary units. (C) EPR kinetics of three biological replicates at pH 11.2 with monoexponential fits (τ is the mean value). The kinetics are normalized to start at zero and to end at the asymptote of the corresponding fits. DEER modulation depths kinetics (green triangles) measured on the first batch of protein. The error bar is $\pm 10\%$ error. (D) Normalized CW EPR kinetics of TcA (1193-IAP) at 2.8 μM TcA pentamer concentration, pH 11.2, and 21°C alone (black) or in the presence of 71 (1:25) and 333 (1:120) μM heparin (green and magenta, respectively). Heparin was used in molar excess to mimic the situation of high heparin concentration on the membrane of the host cell. (E) CW EPR kinetics of TcA (1193-IAP) at 3 μM TcA pentamer concentration at pH 11.2 and 21°C alone (black) or in the presence of 3 μM Vsg (blue). The TcA pentamer-to-Vsg molar ratio is indicated.

S4D), but interaction with Vsg and heparin caused three times and four times increases in pore formation rates, respectively (Fig. 3B and fig. S4, A and F). This indicates that heparin and Vsg play an important role when Tc toxins penetrate directly into host cell membranes at basic pH and suggests that still other factors, such as, for example, yet unknown protein receptors, or a combination of different glycans and protein receptors are needed for Tc toxins acting at acidic pH in the endosomal pathway.

Using EPR, we demonstrated that heparin and Vsg directly increase the probability of shell opening. A 120-fold molar excess of heparin to the TcA pentamer resulted in a 2.3-fold acceleration of shell opening (Fig. 2D and fig. S4, H and I). Incubation with Vsg had a stronger effect (3.6-fold acceleration of the shell opening) at a molar ratio of 1:1 to the TcA pentamer (Fig. 2E and fig. S4, J and K). Thus, binding of Vsg or heparin to TcA is not only involved in docking onto target cells, but it also potentiates the toxin for high pH-induced shell opening. Together, we conclude that the slow shell opening of TcA in vitro can be accelerated by increasingly high pH, liposomes, or receptor binding.

Prepore-to-pore transition proceeds via intermediate states

To study the kinetics of channel ejection in the prepore-to-pore transition (PP*-P, with PP* denoting the prepore state after the pH shift), we could not use CW EPR because no spectral changes were detected after incubation at pH 11.2 (fig. S5A); therefore we performed DEER studies with TcA (914-IAP/2365-IAP) at different incubation times (fig. S5). The shift from pH 7.5 to pH 11.2 resulted in the expected decrease in interspin distance due to channel ejection in the pore state (figs. S1 and S5, B, C, and E), and the DEER kinetics (fig. S5D) unveiled an approximate reaction time $\tau_{\text{PP}^*-\text{P}}$ of 28 ± 8 hours (Fig. 4A), definitely slower than what was detected for the shell opening (Fig. 2C). Therefore, in solution, the formation of the pore is slower (~ 30 hours) than the opening of the shell (~ 11 hours), indicating that there is at least one stable intermediate state (I) between shell opening and channel ejection. Such an intermediate could not be captured by electron microscopy. The pore formation kinetics obtained with negative stain EM data on both TcA (1193-IAP) and TcA (914-IAP/2365-IAP) showed a $\tau_{\text{PP}^*-\text{P}}$ of 10 ± 2 and 11 ± 2 hours, respectively (fig. S6), similar to the kinetics of the

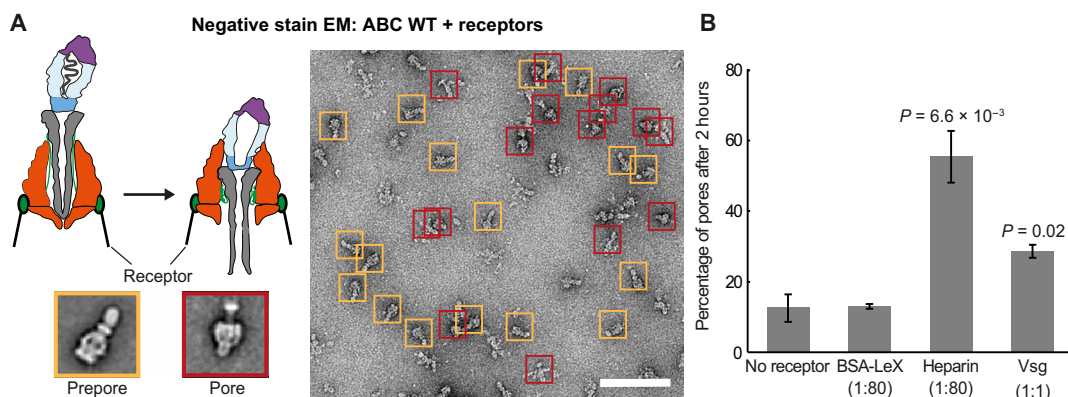


Fig. 3. Negative stain EM analyses of the effect of receptors on prepore-to-pore transition. (A) Left: Scheme of receptor-bound TcA in the prepore and pore states with the respective representative negative stain class averages. Right: A representative negative stain EM image with particles autopicked for quantification of the prepore (orange) and pore (red) particles. Scale bar, 100 nm. (B) Quantification of autopicked pore particles of ABC WT at 70.2 nM pentamer concentration after incubation for 2 hours at pH 11.2 and 21°C, in the presence or absence of the receptors Lewis X (BSA-LeX, 5.8 μM), heparin (5.8 μM), and Vsg (70 nM). The TcA pentamer-to-receptor molar ratios are indicated. The data are presented as mean values, and the error bars represent the SEM of three independent experiments.

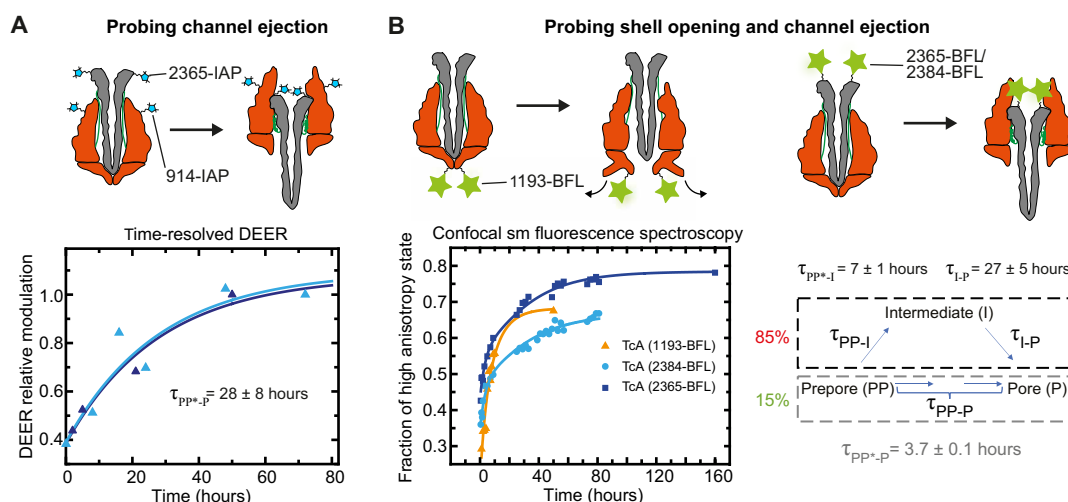


Fig. 4. EPR kinetics and single-molecule fluorescence anisotropy of channel ejection. (A) Top: Design of a TcA variant to probe channel ejection via EPR spectroscopy: TcA (914Cys/2365Cys) was labeled with IAP at both cysteines, resulting in TcA (914-IAP/2365-IAP). Bottom: EPR DEER kinetics at pH 11.2 showing a first-order reaction obtained from a global fit of two biological replicates (light and dark blue data points). For better comparison, data are normalized to the maximum modulation depth achieved. (B) Top: Design of TcA variants to probe shell opening and channel ejection for confocal single-molecule fluorescence anisotropy experiments in solution. TcA (1193Cys), TcA (2365Cys), and TcA (2384Cys) were labeled with BFL-iodoacetamide, resulting in TcA (1193-BFL), TcA (2365-BFL), and TcA (2384-BFL), respectively. Bottom: Confocal single-molecule fluorescence anisotropy experiments in solution at pH 11.2. A model with a consecutive path including one intermediate state and a parallel direct path was needed to describe all three datasets with global rate constants. The three transition rates of model 4 (independent consecutive transitions in note S1, figs. S17 and S18) are shown.

shell opening detected in solution (Fig. 2C), but in disagreement with the DEER kinetics of channel ejection (Fig. 4A). This indicates that the pore formation process of the fraction of toxins trapped on the grid follows the first-order kinetics of the shell opening detected in solution.

To further investigate the origin of the different kinetics observed in solution and to corroborate the data obtained with the spin-labeled variants, we performed additional kinetic experiments in solution using confocal single-molecule fluorescence anisotropy, with different Tc variants labeled with the fluorophore Bodipy-FL (BFL) (Fig. 4B). We monitored shell opening [TcA (1193-BFL)—same labeling position as in EPR] and channel ejection [TcA (2365-BFL) and TcA

(2384-BFL)—different labeling positions as in EPR] (Fig. 4B based on the analysis in fig. S7). The ensemble kinetics derived from the single-molecule anisotropy in solution confirmed faster kinetics for shell opening (orange fit in Fig. 4B) and longer nonmonoexponential kinetics for channel ejection (cyan and blue fits in Fig. 4B). Global analysis of all three experiments allowed us to resolve the presence of at least one stable prepore-to-pore transition intermediate (I) by using a simple consecutive model (Fig. 4B, right). We obtained a reaction time for the prepore-to-intermediate transition ($\tau_{PP \rightarrow I}$) of 7 ± 1 hours and a second reaction time for the intermediate-to-pore transition ($\tau_{I \rightarrow P}$) of 27 ± 5 hours (Fig. 4B, right). However, small deviations at short times indicated the presence of a small fraction of TcAs

(15%) with a direct fast transition from prepore to pore of $\tau_{pp \rightarrow p} = 3.7 \pm 0.1$ hours, as outlined in note S1 (figs. S17 and S18). These observations are in line with observations in experiments (30) and all atom molecular dynamics simulations (31) that a protein has many degrees of freedom resulting in near-isoenergetic states, which immediately leads to multiple pathways for a conformational transition to other states.

Individual transitions: Heterogeneous shell opening and spontaneous channel ejection

To investigate the transition pathway of individual toxins in the ensemble, we immobilized the Tc toxins via biotinylation on neutravidin-coated coverslips and performed single-molecule Förster resonance energy transfer (smFRET) in a total internal reflection fluorescence (TIRF) setup. We used TcA labeled with Atto647N-iodoacetamide at position C1279 [TcA (1279-At647N)] to probe shell opening by homoFRET and a combination of a BFL-labeled TcA [TcA (914-BFL)] and an Atto647-labeled TcB-TcC [TcB (1041-At647N)-TcC] to trace channel ejection by heteroFRET (Fig. 5A and figs. S8 to S9). Additional confocal single-molecule FRET studies confirmed the findings in the TIRF experiments (fig. S10).

We recorded shell opening traces of single Tc toxins and measured transition times from 60 ms to 1.6 s after an initial lag phase

(pretransition time) following pH change (Fig. 5, B to D; fig. S9; and Materials and Methods). The analysis clearly showed that the distribution of transition times was quite broad, indicating that shell destabilization and opening did not happen abruptly but involved small intermediate steps instead. Notably, the pretransition and reaction times are correlated in duration [note S3 (figs. S22 and 23)] so that both processes (Fig. 5F) influence the overall reaction time.

For channel ejection, all detected single reactions showed a transition time within the temporal resolution of the experimental setup (60 ms; Fig. 5, B, C, and E, and figs. S9 and S10). This clearly demonstrates that channel ejection is a spontaneous reaction, resulting from a concerted compaction of all five linkers. The pretransition phase after pH change was longer for channel ejection than for shell opening (Fig. 5B), indicating that the channel is only released after the shell has opened. Thus, the overall reaction time is essentially determined by the pretransition time (Fig. 5F).

Markedly, the overall reaction times extracted from the biotinylated TcA variants confirmed that the kinetics of the overall pore formation were slower than shell opening, as previously observed by EPR and anisotropy measurements, corroborating the existence of one intermediate. However, quite unexpectedly, the reaction times in this setup were about four orders of magnitude faster than the times observed initially (Figs. 4 and 5F), indicating that biotin labeling has

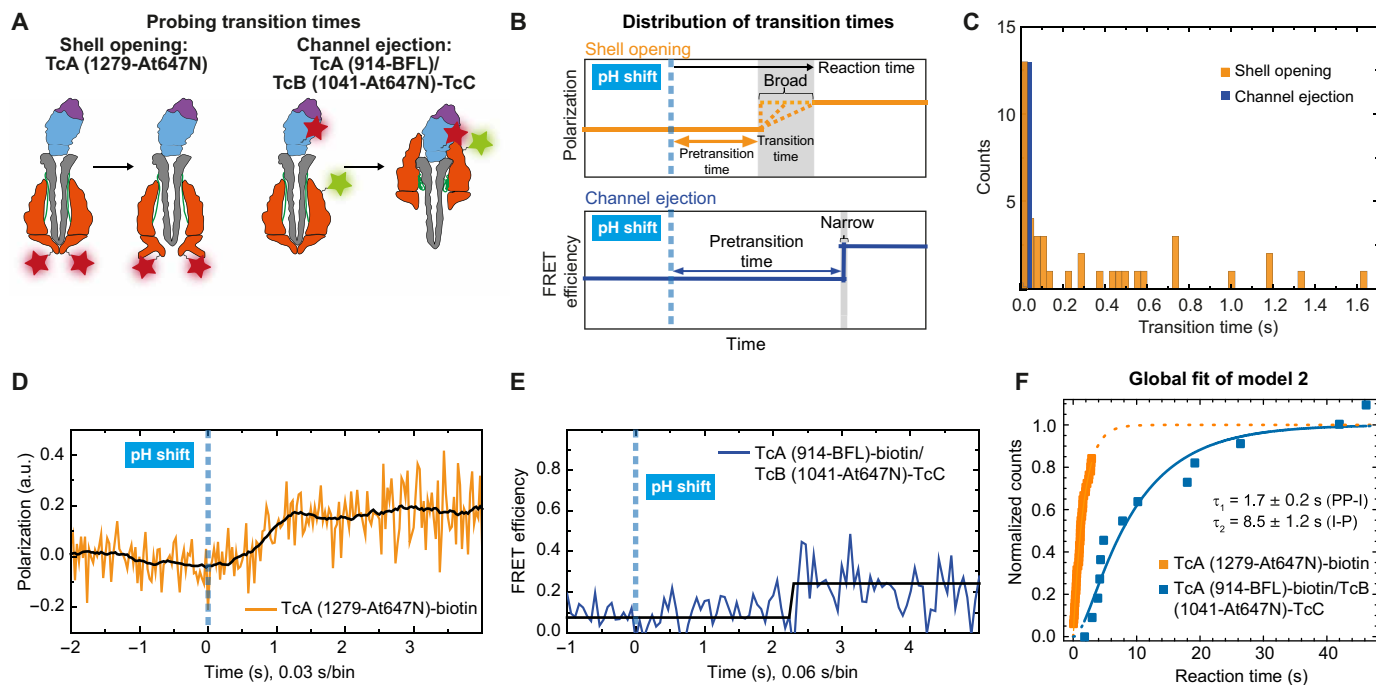


Fig. 5. Total internal reflection single-molecule fluorescence studies of shell opening and channel ejection of surface immobilized toxins. (A) Design of TcA and TcB-TcC variants to probe single shell opening and channel ejection events. (B) Schematics of fluorescence traces probing shell opening (orange) and channel ejection (blue). After a pH jump from 7.4 to 11.2 (blue dashed line, time = 0), the toxin undergoes a transition from the prepore to pore state (shaded in gray) after a specific pretransition time (double-sided arrows). (C) Single-molecule fluorescence homoFRET experiments using biotinylated TcA (1279-At647N) to assess shell opening and channel ejection. Shell opening experiments (42 traces) revealed a distribution of the recorded transition times over 1.6 s (orange bars), whereas those of channel ejection (13 traces) showed transition times within a single frame, below 60 ms (blue bar). (D) A representative shell opening trace using biotinylated TcA (1279-At647N) which reveals transition times longer than the bin width of 29.44 ms and a change in polarization caused by a difference in homoFRET and reduction of dye mobility due to the moving RBDs. (E) A representative trace of the channel ejection heteroFRET assay using ABC with a donor dye at TcA (914-BFL) and acceptor dye at TcB (1041-At647N)-TcC. The displayed trace shows a fast transition of the signal from the prepore to pore state within one bin (bin width = 58.88 ms). (F) Global fit model 2 [see note S1 (figs. S17 and S18), only consecutive]: reaction times of immobilized, biotinylated TcA (1279-At647N) (orange) and ABC composed of TcA (914-BFL)-biotin and TcB (1041-At647N)-TcC (blue). PP, prepore; I, intermediate; P, pore.

a destabilizing effect on the shell at pH 11.2 and thereby strongly accelerates shell opening.

Shell destabilization accelerates prepore-to-pore transition

To understand the role of the biotinylation itself on the acceleration effect, we performed negative stain EM and single-molecule confocal fluorescence anisotropy measurements on biotinylated toxins in solution (fig. S11). Biotinylation had an accelerating effect also in solution as judged by negative stain EM (60% versus <10% of pores formed after a 2-hour incubation at pH 11.2; fig. S11A). In addition, although slower kinetics (hours) were still observed for the channel ejection (fig. S11C), biotinylated TcA showed a quasi-instantaneous increase in the fraction of high fluorescence anisotropy both for the shell opening (fig. S11B) and the channel ejection (fig. S11C), which agrees well with the single-molecule TIRF (smTIRF) microscopy on immobilized toxins (Fig. 5F). Therefore, the comparison of both single-molecule experiments, free in solution and immobilized on surfaces, leads to the consistent finding that biotinylation has an accelerating effect on the prepore-to-pore transition. While in smTIRF microscopy the observation time is limited to a few seconds due to photobleaching of the fluorophores, the confocal anisotropy experiment and negative stain EM resolve the slower toxin fractions on the timescale of minutes to hours so that the faster transitions accumulate in the first data point after the pH jump as indicated by the arrows in fig. S11 (B and C). Notably, biotin labeling of surface-exposed lysines by an *N*-hydroxysuccinimide (NHS) ester was unspecific with respect to the reaction sites and to the number of labeled TcA protomers. Thus, we can expect samples which are heterogeneous with respect to the degree of labeling and the resulting kinetic properties.

Thus, to further address the effect of biotinylation on prepore-to-pore transition in a more specific manner, we produced mimics of biotinylation by site-directed mutagenesis and determined their kinetics in solution. To this end, we specifically focused on electrostatic interactions that involve surface-exposed lysines (NHS-biotin targets) near protomer-protomer interfaces of the TcA pentamer. We chose promising lysines at three different positions of the protein complex: K567 on the α -helical domain of the shell, K1179 on the neuraminidase-like domain near the tip of the channel, and K2008 on the linker (fig. S12A). Although none of these residues are conserved in the Tc toxin family, they are involved in polar and electrostatic interactions potentially stabilizing the conformation of the prepore state of TcdA1 from *P. luminescens* (fig. S12B). Since biotinylating these lysines would neutralize their charges, we mutated the chosen lysines to tryptophan, which also mimics the size increase by biotinylation.

We first focused on the mutants K567W and K2008W and counted the number of pores formed after 2 hours of incubation at pH 11.2 by negative stain EM (Fig. 6A and fig. S12, C and D). Both mutations had an accelerating effect, and the number of pores was three to four times higher compared with the wild type (WT). The number of pores after 2 hours of incubation of the K2008W mutant was comparable to that obtained with the nonspecifically biotinylated protein (fig. S11A). The double-mutant K567W/K2008W did not have the expected amplifying effect, and the number of pores was comparable to the K2008W mutant (Fig. 6A and fig. S12, C and D). In line with the EM study, the K567W/K2008W double mutant showed three times faster kinetics of shell opening in EPR measurements compared to the WT (Fig. 6B and fig. S13, A and B). The

K2008W mutation also accelerated the speed of intoxication of HeLa cells considerably, while K567W showed no difference to the WT (fig. S12E). Together, our results demonstrate that the accelerating effect of biotinylation can be partially mimicked in vitro and in vivo by point mutations that destabilize the shell at different positions.

We then analyzed the mutant K1179W. K1179W had the opposite effect to the other mutants, and we almost did not find any pores after 2 hours at pH 11.2 (Fig. 6A and fig. S12C), and time-resolved EPR measurements confirmed that the TcA shell did not open (Fig. 6B and fig. S13, C and D). In addition, this mutant was not able to intoxicate HeLa cells (fig. S12E). Thus, K1179W stabilizes the closed state of the shell independent of the pH.

However, using a fluorescence quenching assay (Fig. 6C) and polarization-resolved fluorescence correlation spectroscopy (pFCS) (Fig. 6D) (32) on the BFL-labeled K1179W variant [TcA (1193-BFL-K1179W)], we could identify a near-instantaneous (10 ± 0.5 min) local conformational change of the labeled neuraminidase-like domain with a large angle of motion and a unique fast wobbling time t_{wobble} of 100 ns, which is approximately one order of magnitude faster than the global rotational diffusion time $t_{\text{global}} \approx 2.2$ μ s for the toxin particle (1.4-MDa TcA) (see Materials and Methods). This transient local flexibility is related to the pH-induced destabilization of the tip of the shell and is in agreement with the broader distance distribution observed by DEER on TcA (1193-IAP-K1179W) immediately after snap freezing of the sample at pH 11.2 (fig. S13D). At later measurement times (4700 to 5200 s), this transient intermediate (TI) TcA species has vanished, and a more rigid state with t_{wobble} of 600 ns with a smaller angle of motion was formed, which was stable at our experimental conditions (Fig. 6, C and D, and fig. S13, E and F). The stabilization could explain the small decrease in the shell dynamics observed within the first hour of incubation by CW EPR (Fig. 6B). Since this mutant does not form pores, its stabilization must result in a stable intermediate state in which the shell is partially modified but not yet open. Therefore, we call this state stable intermediate 1 (SI1). Notably, EPR (fig. S13D) and fluorescence anisotropy measurements (fig. S13, E and F) found that the neuraminidase-like domain is in its prepore conformation in SI1, corroborating the notion that the initial flexibility in TI is transient.

Prepore-to-pore intermediate with displaced RBDs

To determine the structure of the stable intermediate state SI1, we performed a single-particle cryo-EM analysis at pH 11.2 of the K1179W and K567W/K2008W mutants, as well as a WT-like control TcA protein [TcA (1279-At647N)] (figs. S14 to S16). Expectedly, for the K1179W mutant, only 1% of the toxin was in the pore state, and the rest of the particles resembled prepores but were more slender in appearance (fig. S14, A and B). Two-dimensional (2D) classes of these particles appeared to have protruding densities, implying conformational changes (movie S1). To elucidate the conformation of these particles, we determined their 3D structure at an average resolution of 2.9 Å (Fig. 7A and fig. S14, C and F). The overall conformation is similar to the prepore state, and the tip of the shell is closed below the channel (fig. S13, G to I). However, RBD A is flipped out by about 20° away from the shell, and in line with the slimmer shape, the N-terminal 80 residues and densities corresponding to RBDs B and C are not resolved in the cryo-EM map, indicating that these domains are highly flexible (Fig. 7, A and B, and movie S2). This was also supported by a variance analysis of the cryo-EM density map, which indicated the presence of disordered

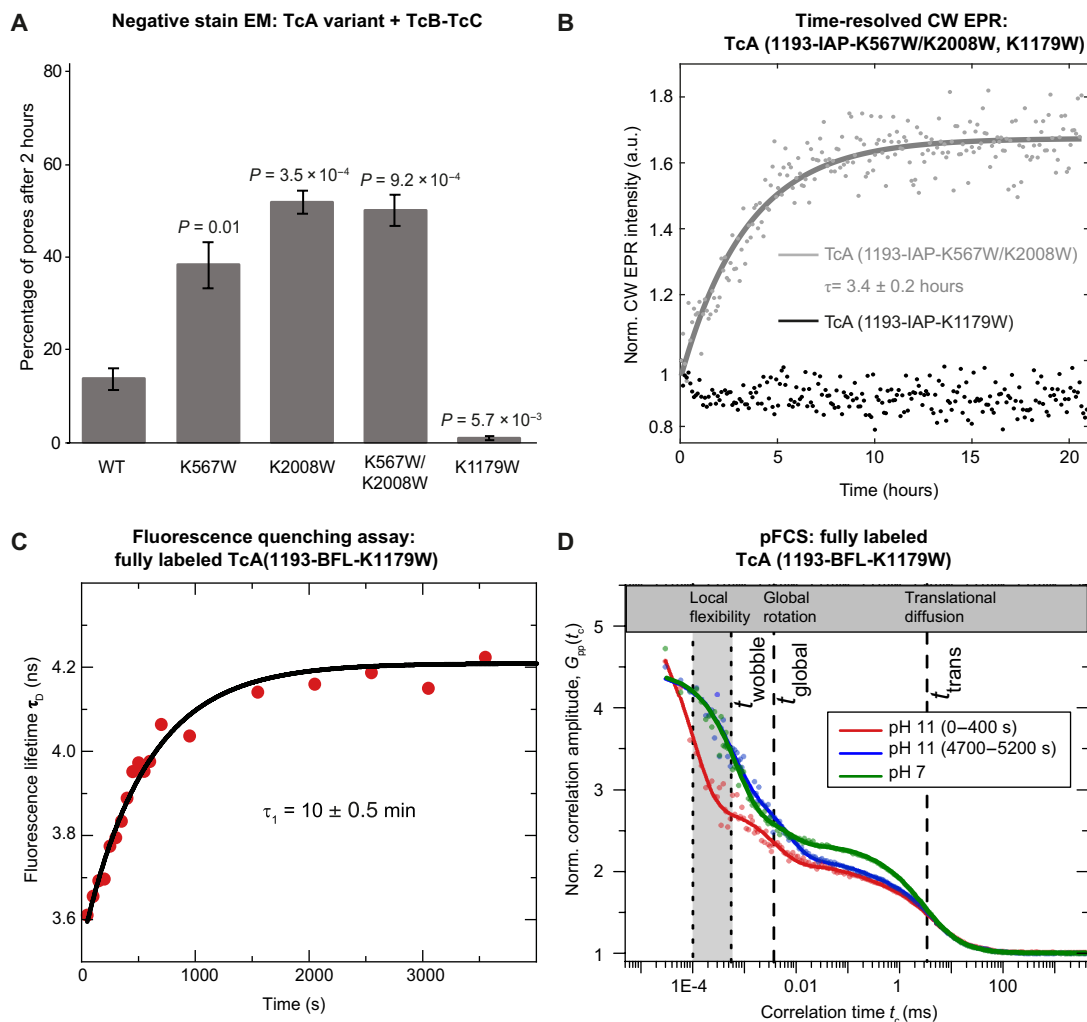


Fig. 6. TcA prepore-to-pore stable intermediate kinetics. (A) Negative stain EM analysis of pore formation of the indicated K-to-W TcA variants with TcB-TcC after incubation for 2 hours at pH 11.2 and 21°C. The data are presented as mean values, and the error bars represent the SEM of three independent experiments. (B) CW EPR kinetics of TcA (1193-IAP-K567W/K2008W) and TcA (1193-IAP-K1179W) at pH 11.2. The shell opening in TcA (1193-IAP-K567W/K2008W) proceeds according to a first-order reaction with a reaction time of 3.4 ± 0.2 hours. The shell in TcA (1193-IAP-K1179W) remains closed, but we observe a small decrease in the label's dynamics within the first hour. (C and D) Confocal multiparameter fluorescence detection (MFD) experiments analyzed by polarization-resolved fluorescence correlation spectroscopy (pFCS) and anisotropy measurements of TcA (1193-BFL-K1179W) at pH 11.2, at longer (C) and shorter incubation (D). (D) pFCS resolves the fast-wobble dynamics of TcA (1193-BFL-K1179W). Experimental data (dots) and fit curves (full lines; see Materials and Methods) for the autocorrelation amplitude $G_{pp}(t_c)$ of parallel polarized fluorescence of TcA (1193-BFL-K1179W) at different incubation times and pH conditions: incubation time of start (0 to 400 s) at pH 11 (red curve), incubation time of measurement end (4700 to 5200 s) at pH 11 (blue curve), and for comparison at pH 7 (green curve) [see note S2 (global fits in figs. S19 to S21 with results in tables S7 to S10)].

regions at the bottom of the outer shell. We therefore applied focused 3D classification and identified a major class with density below the bottom of the shell (fig. S14F). The density corresponds to RBD B (Fig. 7, A and B), but in contrast to the prepore conformation, the domain is flipped by 180° away from the shell. RBD C which is directly connected to RBD B is not resolved, indicating a flexible hinge between the domains. Thus, a shift from pH 7.5 to pH 11.2 induces a conformational change, resulting in a stable intermediate state in which the interaction between the RBDs A, B, and C, and the shell is destabilized and the RBDs are released from the shell. This stable intermediate would normally proceed further to the pore. However, the tryptophans at position 1179 form strong hydrophobic bonds with neighboring phenylalanines at position 2145 and 2147 on the channel, which change their orientation from

their WT conformation (facing down) to that in the mutant (facing up) (fig. S13, G to I) and thus block the opening of the neuraminidase-like domain for pore formation.

To demonstrate that this intermediate state with a destabilized shell and flipped-out RBDs is not only an effect of K1179W, we performed a single-particle cryo-EM analysis of the TcA variant previously used to probe shell opening [TcA (1279-At647N)]. In this case, we decreased the incubation time of the sample to 6 hours at pH 11.2 to favor the population of the intermediate states. We found that 65% of the toxin were in the pore state, but the rest of the particles resembled the intermediate state S11 observed for the K1179W mutant (Fig. 7A and fig. S15A). The 3D reconstruction showed the same overall conformation including the flexible rearrangement of the RBDs (fig. S15, D to F), confirming that this intermediate is also

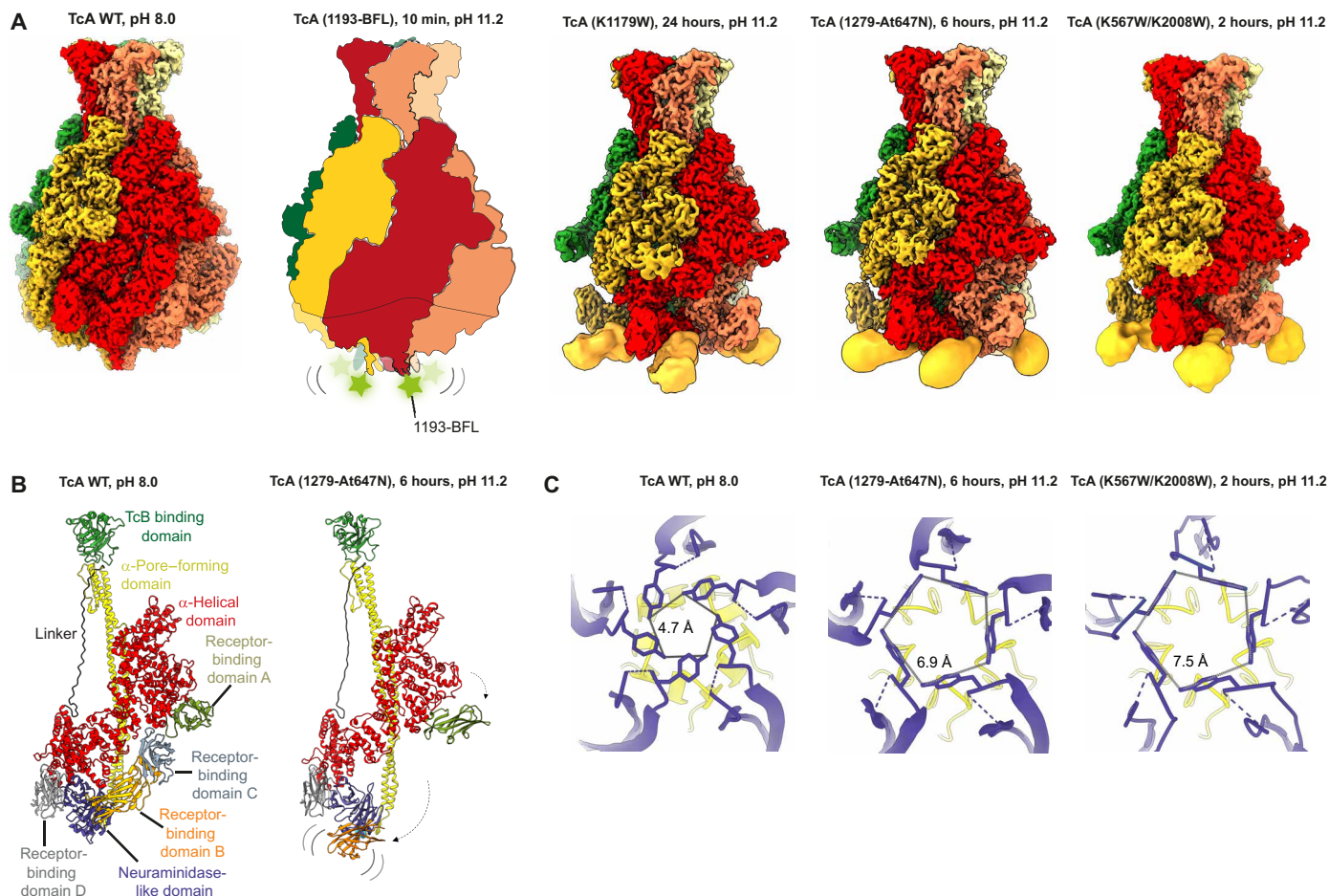


Fig. 7. Cryo-EM structure of the TcA prepore-to-pore stable intermediate. (A) From left to right: Cryo-EM density map of TcA WT at pH 8.0 (EMDB 10033); schematic representation of TcA (1193-BFL) incubated for 10 min at pH 11.2; cryo-EM density map of TcA (K1179W), intermediate state (SI1) after 24 hours of incubation at pH 11.2 and 21°C; cryo-EM density map of TcA (1279-At647N), intermediate state (SI1) after 6 hours of incubation at pH 11.2 and 21°C; and cryo-EM density map of TcA (K567W/K2008W), intermediate state (SI1) after 2 hours of incubation at pH 11.2 and 21°C. TcA (1279-At647N) is a WT mimic that was modified and labeled at position 1279 (see Materials and Methods). The five protomers are colored individually, and the extra density observable at the low binarization threshold (figs. S14 to S16) is shown in orange. (B) Comparison of a protomer of the TcA WT prepore (left; PDB 6RW6) and of the TcA (K1179W) (right) prepore-to-pore intermediate. (C) Bottom view of the TcA WT prepore model at pH 8.0 (PDB 6RW6) (left) compared to the TcA (1279-At647N) (middle) and TcA (K567W/K2008W) (right) intermediate state (SI1) models at pH 11.2. The panels show the average inter-residue distances between Y1188 residues at the tip of the neuraminidase-like domain (purple), which keeps the TcA shell closed. The intermediate states show higher inter-residue distances compared to the prepore, indicating a preopening of the shell. The channel (α -pore-forming domain) is colored yellow.

present in the transition pathway from the prepore to pore state in the WT Tc toxin. An additional cryo-EM structure of the K567W/K2008W double mutant at pH 11.2 also showed the same prepore-to-pore intermediate state; however, the incubation in this case had to be reduced further to 2 hours due to the faster kinetics of pore formation (Fig. 7A and fig. S16). Compared to the WT prepore, the TcA (1279-At647N) and K567W/K2008W intermediates showed an increased diameter at the tip of the neuraminidase-like domain (Fig. 7C), indicating a preopening of the shell at this step, which would continue to open with longer incubation at pH 11.2, ultimately allowing channel ejection and pore formation.

We therefore conclude that in TcA WT there is an intermediate state SI1, in which the RBDs are flipped out but the shell is still closed. Consequently, there must be also an additional and subsequent intermediate state SI2 in which, as we have demonstrated by EPR distance changes, the shell is open but the channel is not yet

released. Unexpectedly, we were unable to trap this state in cryo-EM, suggesting that it is less stable under the plunge-freezing conditions used in cryo-EM, as well as the grid preparation process for negative stain EM.

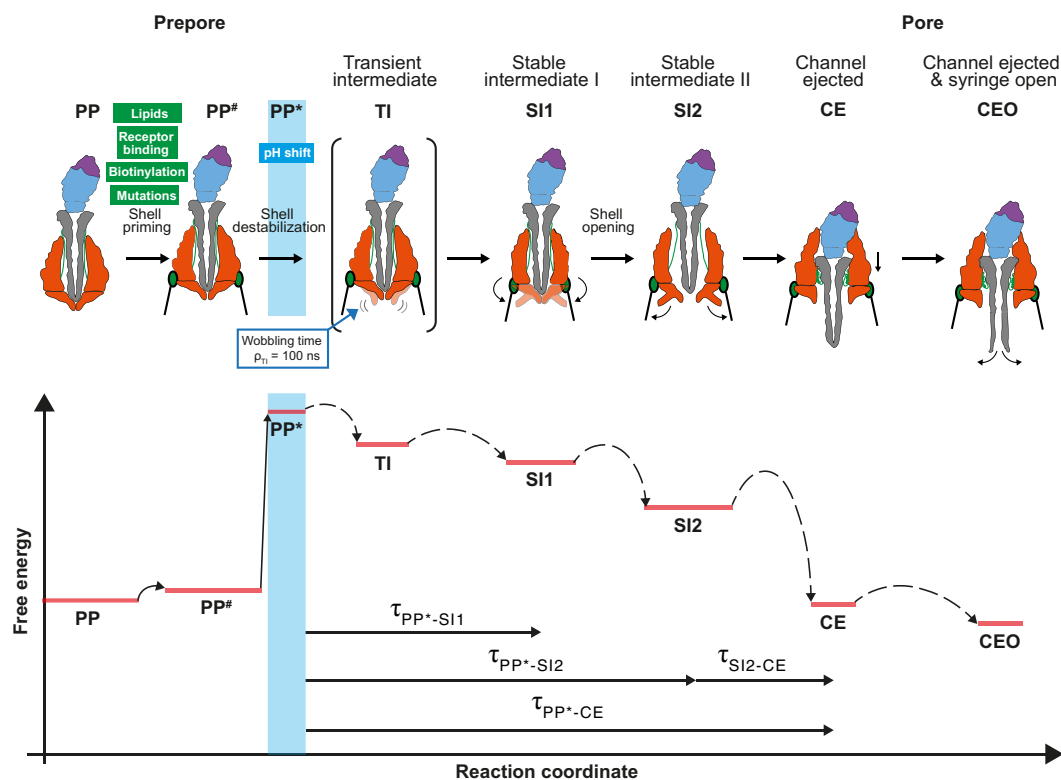
DISCUSSION

Our integrated biophysical approach combining experimental conditions in solution (fluorescence and CW EPR spectroscopy) and in frozen state (DEER and cryo-EM) sets a new standard in the understanding of molecular machines by linking structural and kinetic information. We addressed the challenge of getting local information in large multisubunit protein complexes by specifically attaching probes in subunits to monitor reaction coordinates of interest (shell opening and channel ejection) and build the reaction times of the conformational changes. We compared ensemble kinetics in

solution, obtained via EPR and fluorescence spectroscopies, with the reaction kinetics of individual toxins obtained via single-molecule fluorescence, thus elucidating the role of pretransition times in setting the probability of initiating the different reaction steps.

This multimodal approach enabled us to describe in detail three intermediate states (one transient and two stable) within the syringe-like injection mechanism of Tc toxins (Fig. 8). At neutral pH, the shell of TcA is tightly closed, keeping the channel in its prepre conformation and the RBDs are attached to the α -helical domain of the shell. However, upon a pH increase, a TI is formed, where the neuraminidase-like domain becomes flexible for approximately 400 s (Fig. 6D). The flexibility of the domain is characterized by a wobbling time of 100 ns, which is approximately one order of magnitude faster than the global rotational diffusion time of the toxin particle.

This allowed us to measure flexibility in a large protein complex (1.4 MDa) in a time range that is, to our knowledge, experimentally inaccessible to other methods. This initial step is key for the release and flipping out of the RBDs by disrupting intra- and interprotomer contacts and leads to the SI1 within ~1 hour. Here, the shell is still closed (Fig. 7A). To our knowledge, this rearrangement of the RBDs in an intermediate state is unique for Tc toxins. The RBDs might become accessible to receptors on the host membrane through this flipping movement. However, it is also conceivable that the movement of the RBDs bound to membrane-anchored receptors would result in a lever-like opening of the shell *in vivo*. In any case, we found direct evidence that activation in form of a pH increase is necessary to induce flexibility that is a prerequisite for subsequent conformational transitions.



Reaction time	$\tau_{PP^{\#}-SI1}$	$\tau_{PP^{\#}-SI2}$	τ_{SI2-CE}
WT	10 ± 0.5 min (increase in fluorescence lifetime, Fig. 6C)	11 ± 1.5 hours (increase in EPR dynamics, Fig. 2C)	28 ± 8 hours (approximation with monoexponential fit, DEER distances, Fig. 4A)
		7 ± 1 hours (increase in fluorescence anisotropy, Fig. 4B)	27 ± 5 hours (increase in fluorescence anisotropy, Fig. 4B)
	$\tau_{PP^{\#}-CE}$		
	3.7 ± 0.1 hours (increase in fluorescence anisotropy, 15% probability in Fig. 4B)		
	$\tau_{PP^{\#}-SI1}$	$\tau_{PP^{\#}-SI2}$	τ_{SI2-CE}
WT + heparin (1:120)	n.d.	4.4 ± 0.2 hours (increase in EPR dynamics, Fig. 2D)	n.d.
WT + Vsg (1:1)	n.d.	2.8 ± 0.1 hours (increase in EPR dynamics, Fig. 2E)	n.d.
WT biotinylated and immobilized	n.d.	1.7 ± 0.2 s (increase in fluorescence polarization, Fig. 5F)	8.5 ± 1.2 s (increase in FRET efficiency, Fig. 5F)

Fig. 8. Consecutive model of shell destabilization, opening, and channel ejection. **Top:** Scheme of the transition steps. **Middle:** A qualitative energy landscape depiction of prepre-to-pore transition and reaction times (τ) of the transition steps which are summarized in the table below the scheme. PP, prepre ground state; PP#, primed prepre state; PP*, primed prepre state after pH shift; TI = transition intermediate with flexibility at the neuraminidase domain; SI1, stable intermediate 1 with flipped-out RBDs A, B and C; SI2, stable intermediate 2 with flipped-out RBDs and an open shell; CE, channel ejected pore state with a closed channel tip; CEO, channel ejected pore state with an open channel tip. **Bottom:** Table showing reaction times involving stable intermediates. n.d., not determined.

In the WT, the formation of the SI2 with an open shell has a reaction time of ~10 hours, indicating a low probability of the reaction to be initiated. This intermediate state of the toxin with an open shell but not yet ejected channel exists in solution but could not be visualized by cryo-EM. Overall, the transition from the prepore to the pore state [channel ejected (CE) state] has a reaction time of ~30 hours in vitro with channel ejection being the rate-limiting step for WT. Notably, we also revealed a small fraction of toxins (15%) with a faster and direct overall reaction time of ~3.7 hours. This kinetic heterogeneity is also visible in single-molecule fluorescence traces monitoring the transitions of biotinylated WT molecules immobilized via neutravidin. After a short lag phase, the shells of individual toxins open rather continuously in a broad range of reaction times from 60 ms to 1.6 s, which confirms the presence of fast and slow toxins in this step (Fig. 5C). We found a substantial (50%) fraction of toxins with long transition times, which indicates limited cooperativity between the protomers for the overall process [see correlation between times in note S3 (figs. S22 and S23)]. This kinetic heterogeneity is a hallmark for single protein molecules with many degrees of freedom for functionally relevant transitions (33). On the contrary, the channel ejection has a long lag phase, but then this transition happens instantaneously in a single step within our time resolution of 60 ms for all molecules. The channel ejection of biotinylated WT is rate limiting (reaction time of 8.5 s) (Fig. 5F). This indicates that channel ejection is a spontaneous reaction, in which all five linkers must compact at the same time. Last, as we previously showed, once the channel ejects (CE state), it enters the host membrane where its tip undergoes a conformational change, inducing the opening of the channel (CEO state) (25).

We have directly demonstrated that the high pH shift-induced destabilization and reorganization of the shell are accelerated by the interaction of the toxin with membranes and receptors in vitro. This acceleration is likely increased in vivo due to the combination of various lipids and receptors and their higher local concentration in the membrane. The accelerating effect of receptors can be mimicked by destabilizing the shell through biotinylation or site-directed mutagenesis of lysines at the protomer-protomer interface. Since the shells of these mutants or biotinylated toxins were closed at neutral pH, the lysines cannot be involved in an electrostatic lock. This is in line with our previous conclusion that TcAs, in general, do not have a classic pH switch (14). Instead, the lysines are rather involved in a general stabilization through polar and electrostatic interactions either within domains or between the shell domains of two protomers, and their modification destabilizes the shell and accelerates its opening at high pH similar to the interaction with receptors. These mutants could be of use in obtaining better functioning and perhaps more applicable toxin varieties for clinical therapies and/or biological insect pest control.

In contrast, stabilizing modifications of specific protomer-protomer interactions, as in the case of the K1179W mutant, result in the blocked SI1 that cannot be opened even after destabilization of the shell at high or low pH and thus cannot intoxicate cells. Antibodies or nanobodies that would mimic this stabilizing mutant and prevent shell opening would be ideal antidotes against Tc toxins of human pathogenic bacteria.

MATERIALS AND METHODS

Design of TcA variants

P. luminescens TcdA1 (TcA) WT contains 10 cysteines per protomer, three of them being surface-exposed (C16, C20, and C870) and thus

expected to interfere with site-specific labeling for EPR spectroscopy and smFRET spectroscopy experiments. In this regard, we mutated the three cysteines to serines via QuikChange polymerase chain reaction (PCR). The labeling of this variant with twofold nitroxide spin labels under conditions described below did not result in a detectable CW EPR signal, indicating that the remaining cysteines are inaccessible. The obtained variant, TcA (C16S/C20S/C870S), therefore served as the basis for all TcA variants subsequently designed for labeling with iodacetamido-PROXYL (IAP), BFL-iodoacetamide, and Atto647N-iodoacetamide (At647N).

We next introduced a cysteine at position 1193 at the bottom of the shell to follow shell opening of TcA (fig. S1A) or two cysteines at positions 914 and 2365 (upper part of the shell and the funnel, respectively) to follow channel insertion (fig. S1B), resulting in TcA (1193Cys) and TcA (914Cys/2365Cys). These TcA variants served for subsequent labeling with IAP for EPR and BFL for smFRET.

To label TcA with BFL and Atto647N for smFRET and fluorescence polarization experiments, we created TcA (1279Cys) and TcA (914Cys) analogously. In addition, we introduced a cysteine at position 1041 of *P. luminescens* TcdB2-TccC3 (TcB-TcC), resulting in TcB-TcC (1041Cys) to attach Atto647N.

To mimic biotinylation of TcA at different surface-exposed lysines, we first assessed the protein for all surface-exposed lysines, particularly focusing on those near protomer-protomer interfaces. For this, we used the H++ server (newbiophysics.cs.vt.edu/H++) (35) to predict the electrostatic landscape of TcA at pH 11. Both the WT model [Protein Data Bank (PDB) 6RW6] and models where a chosen lysine was changed to a tryptophan were used for the prediction. Since biotinylating the exposed lysines would neutralize them, we mutated the chosen lysines via QuikChange PCR to tryptophans. Tryptophan was chosen because it comes closest in size to biotin. Of those observed lysines, three were selected that are near protomer-protomer interfaces: K567 at a lysine cluster on the shell, K1179 on the neuraminidase-like domain near the tip of the channel, and K2008 on the linker (fig. S12, A and B). Mutation resulted in the TcA (K567W), TcA (K1179W), and TcA (K2008W) variants used for negative stain EM and cryo-EM, as well as cell cytotoxicity. Furthermore, a double mutant with K567W and K2008W, TcA (K567W/K2008W), was further mutated to add 1193Cys or 914Cys/2365Cys for EPR measurements. Similarly, TcA (K1179W) was mutated to add either 1193Cys for EPR and smFRET measurements or 2365Cys for smFRET measurements.

For single-particle cryo-EM analyses of prepore-to-pore transition intermediates, some key TcA variants were selected, namely, TcA (1279-At647N) which served as a WT/control for cryo-EM experiments as it showed WT-level prepore-to-pore transition kinetics in single-molecule experiments; TcA (K1179W) which showed almost no transition to the pore state in EM, EPR, and smFRET experiments; and ABC (K567W/K2008W) which showed a considerably increased rate of prepore-to-pore transition in the mentioned experiments. The TcA variants TcA (K1179W) and TcA (K567W/K2008W) in ABC (K567W/K2008W) were both based on the unmodified TcA WT and therefore lacked the modifications made for variants designed for labeling. All three datasets were collected on proteins incubated at pH 11.2 as described in the subsequent sections.

Protein production

TcA (WT and all variants) and TcB-TcC [WT and TcB-TcC (1041Cys)] were expressed in BL21-CodonPlus (DE3)-RIPL in 10 liters of LB

medium and purified as described previously (24). All variants of TcA were expressed and purified like TcA WT with the exception that 0.5 mM tris(2-carboxyethyl)phosphine (TCEP) was present in all purification buffers to keep all surface-exposed cysteines in reduced state. The extracellular, highly O-glycosylated domain of Vsg was produced and purified as previously described (18), with an additional desalting step into 20 mM Hepes (pH 7.5), 150 mM NaCl, and 0.05% Tween 20 using a PD Spin-Trap G-25 desalting column (Cytiva).

Spin labeling of TcA for EPR studies and determination of labeling efficiency

Immediately before labeling, TcA variants were buffer-exchanged to labeling buffer [10 mM Hepes-NaOH (pH 7.5), 150 mM NaCl, and 0.05% Tween 20] and concentrated to at least 5 μM (protomer concentration). We used IAP (Sigma-Aldrich, catalog no. 253421) for labeling because it sustains highly basic pH values necessary for this study without the drawbacks of commonly used *S*-(1-oxyl-2,2,5,5-tetramethyl-2,5-dihydro-1H-pyrrol-3-yl)methyl methanesulfonothioate (36) or maleimide-functionalized labels (37). For TcA (1193Cys), a twofold molar amount of IAP per protomer was added, and for TcA (914Cys/2365Cys), a threefold molar amount was added. Labeling was performed for 1 hour at 22°C, followed by overnight incubation at 4°C. Subsequently, unbound IAP was removed by diluting the samples three times 10-fold in labeling buffer and concentrating back to the original volume with an Amicon Ultra 100 kDa cutoff concentrator (Millipore). The protein concentrations for subsequent EPR experiments are given in table S1.

For determination of labeling efficiency, 20 μl of the concentrated samples was pipetted into glass capillaries with 0.7-mm inner diameter (BLAUBRAND). Next, CW EPR spectra were either recorded on a Miniscope MS 5000 (Magnetech, Bruker BioSpin) at X band (9.5 GHz) or on a Bruker X-band (9.8 GHz) E580 (Bruker BioSpin) spectrometer equipped with Bruker super-high Q resonator at an ambient temperature (21°C). Measurement conditions for Miniscope (fig. S1D) were as follows: 10-mW power, 0.15-mT modulation amplitude, 100-kHz modulation frequency, 15-mT sweep width, and 80-s sweep time. Measurement conditions for spectra detected with the Bruker spectrometer (red spectrum in figs. S1D and S13) were the same as given below for the kinetic measurements.

Labeling efficiency was calculated as a percent ratio between the spin concentration and the concentration of introduced cysteines (1193Cys or 914Cys/2365Cys) in the TcA protein (protein concentration determined by the absorption at 280 nm with an extinction coefficient of 400,750 $\text{M}^{-1} \text{cm}^{-1}$ per protomer). Spin concentration was determined from double integration of X-band CW EPR spectra (figs. S1D and S13) by comparison to a standard stock solution of 100 μM 4-hydroxy-2,2,6,6-tetramethylpiperidine 1-oxyl (Sigma-Aldrich) in water measured at the same conditions. The error in spin labeling efficiency taking into account uncertainties in protein concentration and baseline noise-related errors in the double integral value is estimated to be $\pm 10\%$ (38). All labeling efficiencies, as well as corresponding protein and spin concentrations, are listed in table S1.

Labeling of TcA and TcB-TcC for fluorescence polarization and FRET studies

TcA (1193Cys), TcA (1279Cys), and TcA (914Cys) were labeled with the green fluorescent dye BFL or the red fluorescent dye Atto647N for smFRET or fluorescence polarization experiments. For experiments that require one fluorophore per TcA protomer, a twofold

molar excess of label over the protomer concentration was added in labeling buffer [10 mM Hepes-NaOH (pH 7.5), 150 mM NaCl, and 0.05% Tween 20], followed by 1-hour incubation at 22°C and subsequently overnight at 4°C. For experiments that require one fluorophore per pentamer, a 1.1-fold molar excess of label over the pentamer concentration was added and incubated as above. TcB-TcC (1041Cys) was labeled with a twofold molar excess of Atto647N using the same conditions. After labeling, unreacted dye was removed using a Superose 6 increase column equilibrated in 10 mM Hepes-NaOH (pH 7.5) and 150 mM NaCl.

Biotinylation of TcA variants

To immobilize the proteins for TIRF measurements, TcA (914Cys) and TcA (1279Cys) were biotinylated using EZ-link NHS-PEG12-Biotin (Thermo Fisher Scientific, catalog no. A35389). Biotinylation was performed in labeling buffer simultaneously to the labeling reaction with BFL and Atto647N, respectively. NHS-PEG12-Biotin (5.6 μM) was added to 2.8 μM TcA pentamer from a 500 μM stock solution in water-free dimethyl sulfoxide, and the reactions were incubated for 20 min at 22°C, followed by overnight incubation at 4°C. Unreacted biotin was removed analogously to the removal of free IAP label.

Simulation of spin label distances

The expected interspin distances between the chosen sites were simulated by rotamer library analysis with MMM 2018.2 (39, 40) in MATLAB R2017b (MathWorks). To speed up the rotamer library calculations, the amino acids of TcA located at >10-nm distance from the labeling sites were removed from the structure before the simulations. The implemented room temperature rotamer library for IAP was used to calculate the allowed rotamers attached at cysteine-substituted sites. TcA (1193-IAP) revealed 22 allowed rotamers per chain in the prepore state, which increased to 40 to 62 depending on the chain in the pore state. TcA (914-IAP/2365-IAP) showed 35/91 rotamers (prepore) and 29-34/72-77 (pore) for IAP at positions 914 and 2365, respectively. For representation, single rotamers at each site are depicted in fig. S1 (A and B).

The remaining native, not surface exposed cysteines at TcA positions 499, 756, 870, 1149, 1236, 1372, 2273, and 2445 revealed only one to two allowed IAP rotamers. The inaccessibility of these sites was proven experimentally (no detectable CW EPR signal after labeling).

CW EPR kinetic measurements

Ten microliters of labeled TcA in labeling buffer was mixed with 10 μl of measurement buffers (pH 4.0: 100 mM Na-acetate, 150 mM NaCl, and 0.1% Tween 20; pH 7.5: labeling buffer; pH 11.2: 100 mM CAPS-NaOH, 150 mM NaCl, and 0.1% Tween 20), thereby resulting in two times lower final protein and spin concentration as compared to values given in table S1. CW EPR kinetic measurements were performed on a Bruker X-band (9.8 GHz) E580 (Bruker BioSpin) spectrometer equipped with Bruker super-high Q resonator at an ambient temperature. Kinetics were plotted as peak-to-peak intensity of the central spectral line over time (3 to 5 min dead time) normalized as stated in the corresponding legends. The CW EPR kinetics were fitted with a monoexponential function. To facilitate the comparison of the kinetics in Fig. 2 (C to E), the initial fit offset was subtracted, and the data were divided by the fitted asymptote, so that the fits of all plotted data start at 0 and end at 1. Spectra were

recorded with 0.75- to 2-mW power, 0.1- to 0.15-mT modulation amplitude, 100-kHz modulation frequency, 13-mT sweep width, 40-s sweep time, and four or eight averages per scan. CW EPR kinetics were successfully detected on TcA (1193-IAP), which showed increased dynamics of the shell over time within the sensitivity range of X-band EPR (30 ps to 30 ns). No notable changes in the dynamics of the spin labels during the transition from prepore to pore were observed for TcA (914-IAP/2365-IAP). The corresponding time constants of the fits (kinetics at different pH values and in the presence of liposomes) are summarized in table S2. Liposomes used in these experiments were prepared using POPC (Avanti Polar Lipids) as previously described (26). The samples for the kinetic measurement in liposomes were prepared analogously to the standard buffer samples, where 10 μ l of labeled TcA in labeling buffer was mixed with 10 μ l of liposomes at given pH, thereby resulting in two times lower final protein and liposome concentration.

Double electron-electron resonance

Ten microliters of the labeled TcA variants in labeling buffer were mixed with 10 μ l of the different measurement buffers (see above) prepared with 50% (v/v) D₂O and incubated for time intervals between 0 min and 72 hours at 21°C or at 4°C as stated in the corresponding legends. After incubation, 20 μ l of fully deuterated glycerol (glycerol-d₈, Sigma-Aldrich) was added, thereby resulting in four times lower final protein and spin concentration as compared to values given in table S1. Last, the samples were transferred into 3-mm-quartz capillaries (Aachener Quarzglas Heinrich) and shock-frozen in liquid N₂. The overall mixing/freezing time took 2 to 6 min. The final spin concentration in all DEER tubes did not exceed 8 μ M, which minimizes the contribution of intermolecular background and increases the fidelity of the extracted distances. For all pulsed EPR experiments, a Bruker Q-band Elexsys E580 spectrometer equipped with a 150 W TWT amplifier and SpinJet-AWG and a home-made microwave cavity suitable for 3-mm tubes (41, 42) was used. The dead-time free 4-pulse DEER sequence (43) with 16-step phase cycling (44) and Gaussian pulses (45) was used. In addition, eight steps of 16-ns cycling were used for electron spin echo envelope modulation averaging. Shot repetition time was 3 to 4 ms. The interpulse delay d1 was 400 ns, d2 varied in microsecond range between the traces, and 8-ns stepping Δt was used. All Gaussian pulses were optimized via nutation experiments and set to the same length of 32 ns (~13.6-ns full width at half maximum) to achieve the same excitation bandwidth. The pump pulse was applied at the position of maximal microwave absorption of nitroxides. The pump pulse was set with +(90 to 100)-MHz offset from the observer frequency, with both frequencies chosen symmetrically in the microwave dip. All pulsed measurements were performed on frozen samples at 50 K. The total acquisition time varied between the samples in the range 1 to 72 hours for short and long traces, respectively.

DEER data analysis and validation

DEER data were analyzed using Tikhonov regularization or Neural-Net tool (46) with the generic set in DeerAnalysis2019 (47) according to the guidelines (48). The zero time was determined experimentally and set to 120 ns. For Tikhonov regularization, the homogeneous background function with $D = 3$ was chosen for the data shown in fig. S3A to correct for the minor background contribution. For TcA (1193-IAP), both Tikhonov regularization and neural network analysis were used for validation of DEER data in fig. S3C,

showing no notable discrepancies between the methods. Therefore, the supplementary DEER data in figs. S2E, S5 (B and E), and S13D were analyzed and validated using neural networks only.

The accuracy of the measured short distances was further validated by testing the absence of ghost frequencies in the multispin systems of TcA (1193-IAP) and TcA (914-IAP/2365-IAP) by reducing pump pulse with a power scaling factor $\lambda = 0.5$ (figs. S3D and S5C) (49).

DEER “snapshot” kinetics

To obtain time-resolved DEER kinetics, samples were incubated for different times, snap-frozen in liquid nitrogen, and measured. To resolve the small changes in modulation depths, short DEER traces were recorded to reach higher signal-to-noise ratios. The collected sets of primary DEER traces (figs. S3B and S5D) revealed a clear trend of decreasing modulation depths for TcA (1193-IAP) due to the disappearance of the short distances and increasing modulation depths for TcA (914-IAP/2365-IAP) due to the appearance of the short distances upon prolonged incubation at pH 11.2. Thus, to estimate the time constant in both cases, the modulations at the first inflection point were plotted against incubation time. The modulation depth at this point should mainly represent the fraction of Tc proteins in the ensemble characterized by short distances. For the determination of the inflection point, the trace with the most pronounced high-frequency oscillation and the best signal-to-noise ratio was chosen and fitted with a polynomial function in DEER Analysis2019. The first and second derivatives of the obtained polynomial fit were calculated to determine the first inflection point in the time domain. The modulations extracted at this point after different incubation times were normalized to the maximal value for the two batches of TcA (914-IAP/2365-IAP).

Confocal single-molecule fluorescence spectroscopy

Single-molecule measurements with multiparameter fluorescence detection (MFD) were performed on a home-built setup based on an Olympus IX70 inverted microscope as described by Widengren *et al.* (50). To prevent concentration drops due to unspecific adhesion of the molecules, the cover glass was passivated with bovine serum albumin (BSA) using 10 μ M stock solution, which was washed off after 2-min incubation time. An Olympus UPlanSApo 60 \times /1.2 objective was used. A linearly polarized, pulsed diode laser with a wavelength of 495 nm (LDH-D-C 495, PicoQuant) operated at 64 MHz was used. In the case of PIE (pulsed interleaved excitation) configuration (51), an additional red laser with a wavelength of 635 nm was used, both operated at 32 MHz in an alternating order. For detection, the beam is split into parallel and perpendicular polarization and filtered by color using ET 535/50 and HQ 730/140 (AHF Analysentechnik) bandpass filters and, after 50/50 splitting of each channel, detected by eight SPAD detectors. Single photon counting was done with synchronized channels (HydraHarp 400, PicoQuant, Germany) operating in time-tagged time-resolved mode. Burst selection and data analysis were done using established procedures and in-house software described in (52), available upon request on the homepage of the Seidel group (<https://www.mpc.hhu.de/software.html>).

Single-molecule events were identified using a burst search algorithm according to Fries *et al.* (53) using a Lee filter, a threshold of 0.2 ms, and a minimum of 60 photons per burst. For anisotropy photon distribution analysis (aPDA), the whole trace including all bursts was analyzed. For heteroFRET analysis, molecules with a

stoichiometry between $S = 0.5$ and $S = 0.8$ were selected. The labeling geometry of five possible labeling spots for TcA (914-BFL)-Biotin:TcB (1041-At647N)-TcC and labeling scheme of 5:1 donor to acceptor led to a higher than the usual value of the stoichiometry, where multiple donors were attached to the molecule with only one acceptor. However, only one of the label positions had a distance to the acceptor where FRET occurs, giving the possibility to qualitatively measure FRET efficiency-derived distances.

In heteroFRET studies, static FRET lines as described by Kalinin *et al.* (54) were used for consistency and quality control. A static FRET line relates the lifetime of the donor in the presence of an acceptor, $\langle \tau_{D(A)} \rangle_F$, to the intensity-based FRET efficiency, E . In the case of the Tc toxin, no dynamic exchange between conformational states was expected. This matches the experimental data, where the double labeled FRET population of the Tc toxin in prepore and pore states in the $\langle \tau_{D(A)} \rangle_F - E$ relation is located on the static FRET line (see fig. S10).

pFCS (32) was performed by auto- and cross-correlating the two corresponding parallel and perpendicular polarized time traces of the detected photons using in-house software (55). In this way, we obtained three correlation functions: $G_{pp}(t_c)$, autocorrelation function of parallel polarized fluorescence; $G_{ss}(t_c)$, autocorrelation function of the perpendicular polarized fluorescence; and $G_{ps,sp}(t_c)$ average cross-correlation function of parallel and perpendicular polarized fluorescence. Amplitudes and relaxation times of the observed bunching terms (translational diffusion and triplet and rotational diffusion that depended on the reaction time) were extracted by a global fit procedure using a model function to the data applying the same software. The term for rotational diffusion was identified by its characteristic dependence of the amplitude with $G_{pp}(t_c) > G_{ss}(t_c) > G_{ps,sp}(t_c)$. For details, see note S2 (tables S7 to S10 and figs. S19 to S21).

smTIRF microscopy

Imaging was performed on a home-built TIRF setup based on an Olympus IX70 microscope and a charge-coupled device (CCD) camera (emCCD, DU-897D-BV, Andor). Using a special TIRF objective (Apo N 60 \times , 1.49 numerical aperture, Olympus) with very high numerical aperture leads to total internal reflection of the light beam on the surface of the glass. For homoFRET studies, a single color excitation with a 488-nm CW laser (Cobolt MLD) was used. In the case of heteroFRET, an additional 635-nm CW laser (Cobolt MLD) was added using alternating excitation, triggered with a home-built switch. Emission light passes a dichroic mirror and is then split by polarization (homoFRET) or by color (heteroFRET) and projected as two spatially separated images (parallel/perpendicular or green/red, respectively) on the camera using an image splitter

(OptoSplit II, Cairn Research Ltd). Splitting by color was done using a HC BS 580 Imaging beam splitter (AHF Analysentechnik) and bandpass filters (green: HQ 535/50, red: HQ 680/60). Splitting by polarization was done by inserting a polarizing beam-splitting cube. For every measurement, 2048 images with a size of 512×512 pixels were taken with a single frame time of 29.44 ms. Spot selection and data analysis were done using the software iSMS (56). For background subtraction, the mean intensity of a background mask was used. Spot selection was done using an automatized intensity-based algorithm. To calibrate the overlay of the two individual images, a measurement with inhomogeneous areas was used. Polarization traces were smoothed using the Savitzky-Golay algorithm with varying number of points.

HeteroFRET assay for channel ejection

FRET efficiency traces were averaged on the basis of the time interval before and after the transition. The correction factors for the FRET efficiency were calculated on the basis of the spectral properties of the dyes and applied globally for each molecule. The correction factors shown in Table 1 below were used.

For heteroFRET efficiency, background-corrected fluorescence F was used following equations described in section intensity-based MFD. Because of long necessary observation times of up to 40 s, most FRET pairs were bleached during pretransition time. Thus, we could resolve only 13 single reactions with FRET efficiency change before photobleaching.

HomoFRET anisotropy assay for shell opening

Here, one has to take into account that the high numerical aperture of the TIRF objective influences the polarization of the laser beam, leading to a mixture of polarizations. For the same reason, the polarization of the collected fluorescence is partially mixed. In addition, the laser beam enters the solution at an angle greater than a critical angle for total reflection. This effect was studied in detail, and a shift to lower anisotropy values was observed (57, 58). In addition, because of a high amount of different labeling sites of the biotin on the Tc toxin, the initial orientation and therefore polarization values of the toxin were distributed. However, in this assay, the difference of polarization of the signal before and after the transition from prepore to pore was of interest. Therefore, we applied a polarization offset based on the mean polarization value before the pH change (P (pH7)) to every trace shifting the polarization value before the pH change to $P = 0$. The polarization value resulted in $P = \frac{F_{\parallel} - F_{\perp}}{F_{\parallel} + F_{\perp}} - \langle P \text{ (pH7)} \rangle$.

In total, 765 homoFRET pairs were recorded where 48 of them showed a trackable transition, while the rest were either FRET inactive due to the labeling scheme described in table S4 or the dyes were bleached. The time after pH change ($t = 0$) until the signal changes

Table 1. Correction factors calculated based on the spectral properties of the dyes used in heteroFRET experiments.

Correction factors (see Supplementary Methods)	HeteroFRET Alexa488/Atto647N	HomoFRET Atto647N/Atto647N
α	0.016	0
δ	0.02	0
g_{DA}	1.25	1
g_{DD}		
$\frac{eff \Phi_{FA}}{eff \Phi_{FD}}$	$\frac{0.65}{0.8} = 0.81$	1
γ	1.02	1

before the transition starts is defined as the pretransition time (see Fig. 5B). The transition time is defined as the time the signal needs until it is permanently changed. To determine these time points, a binned derivative of the trace was calculated as the change of between two signals over the interval, which was binned afterward with a binning size of two frames.

Immobilization of toxins for smTIRF measurements

Tc toxins were immobilized on the surface using biotinylated BSA. Cleaning of nunc chambers (Nunc Lab-Tek II, thickness no. 1.5H, Thermo Fisher Scientific) was done by activating them in an oxygen plasma for 2 min (Femto Plasma Cleaner, Diener Electronic). After cleaning, the surface was incubated for 10 min with biotinylated BSA [3 mg/ml in phosphate-buffered saline (PBS); Sigma-Aldrich], washed several times with PBS, incubated for 10 min with neutravidin (20 μ g/ml in water; Invitrogen), and washed again with buffer. The biotinylated toxins were then added and incubated for up to 30 min. Lastly, the chamber was washed again to remove diffusing toxins and dyes.

Kinetics of shell opening and channel ejection monitored by single-molecule confocal fluorescence anisotropy measurements

Long confocal fluorescence measurement series were performed with several 10-hour measurements, which were cut into 2-hour intervals for data analysis. The ratio of parallel and perpendicular signals S_{\parallel} and S_{\perp} of each burst of the whole trace was fitted in a time window-based aPDA (55). More details are given in Supplementary Methods. The applied model fitted global values for the ratios/anisotropy with varying fractions. Typical data are shown in fig. S7. Time-dependent fractions were fitted by comparing four distinct kinetic models. See note S1 (figs. S17 and S18) for all details.

Simulation of interfluorophore distances by AV simulations

To design a label scheme with dyes positioned in the FRET-sensitive range to measure the conformational change due to shell opening and pore ejection, a FRET position screening was applied following (59) and using in-house software to find the most promising labeling positions for specified structural models. In short, it simulates for each position so-called sterically accessible volumes (AVs) (52) to a series of positions on the biomolecule while calculating the expected FRET-averaged interdye distance $\langle R_{DA} \rangle_E$ (typical examples are shown in fig. S8). The labeling positions were selected in two steps: (i) To reduce time and effort, the position for the donor dye was set to an already used position for other experiments, and AV simulations were used to suggest positions for the acceptor in a FRET-sensitive range. (ii) Suitable positions were checked for the presence of quenching amino acids in the surroundings (60). Last, the protein was labeled and tested using single-molecule multiparameter fluorescence detection (smMFD). The outcome was that the most sufficient label scheme in terms of good label ratio for shell opening was TcA (1279-At647N) and for pore ejection, TcA [914-BFL:TcB (1041-At647N)-TcC]. The relevant interdye distances and the expected FRET efficiencies of the studied toxin constructs are compiled in table S4.

Cell intoxication

HEK293T cells (Thermo Fisher Scientific) were intoxicated with preformed holotoxin composed of TcB-TcC WT (unmodified) and TcA WT (unmodified), TcA (1193-IAP), or TcA (914-IAP/2365-IAP). A total of 5×10^4 cells in 400 μ l of Dulbecco's modified Eagle's

medium (DMEM)/F12 medium (Pan Biotech) were grown overnight and subsequently intoxicated with 0.5 nM toxin. Incubation was performed for 16 hours at 37°C before imaging. Experiments were performed in duplicate (two biological replicates). Cells were not tested for mycoplasma contamination.

To test the toxicity of TcA biotinylation mimics (K567W, K1179W, and K2008W), HeLa cells (provided as a gift from A. Musacchio) were intoxicated with preformed holotoxins of each TcA mutant and TcB-TcC WT. A total of 6×10^4 cells in 1 ml of DMEM medium (Pan Biotech) were grown for 48 hours before addition of 5.8 nM toxin. The cells were then incubated at 37°C with images acquired at 6, 7, and 8 hours. Subsequently, the number of rounded cells was calculated for each mutant using ImageJ/Fiji (61) as a quantification of cytotoxicity. Experiments were performed in triplicate (three biological replicates). Cells were not tested for mycoplasma contamination. Quantified data were analyzed using an unpaired two-tailed *t* test.

Negative stain EM kinetics

Before pH-induced prepore-to-pore transition, TcA (WT, IAP-labeled variants, and biotin mimics) was mixed with a twofold molar excess of TcB-TcC to form holotoxins [ABC WT, ABC (1193-IAP), ABC (914-IAP/2365-IAP), ABC (K567W), ABC (K1179W), ABC (K2008W), and ABC (K567W/K2008W)]. The resulting ABC holotoxins were then separated from excess TcB-TcC by size exclusion chromatography on a Superose 6 increase 5/150 column (GE Life Sciences) equilibrated in labeling buffer. The prepore-to-pore formation of ABC was then started by mixing a protein (0.1 to 0.2 mg/ml) with 100 mM CAPS-NaOH (pH 11.2), 150 mM NaCl, and 0.1% Tween 20 or 100 mM sodium acetate (pH 4.0), 150 mM NaCl, and 0.1% Tween 20 in a 1:1 ratio. After the indicated time intervals of incubation (1 min to 72 hours), the proteins were applied to glow-discharged copper grids with 8-nm amorphous carbon layer pretreated with/without 0.1% polylysine, stained with 0.75% uranyl formate, and imaged using a Tecnai Spirit transmission electron microscope (Thermo Fisher Scientific) operated at 120 kV and equipped with a TVIPS TemCam F416 detector. Images were recorded at a pixel size of either 1.67 Å/pixel or 2.61 Å/pixel.

For every variant and incubation time, 36 to 64 micrographs were recorded to obtain at least 4000 particle images. To quantify prepores and pores, we trained two models in crYOLO (62) to pick specifically ABC prepores and pores from the EM micrographs, respectively. Subsequently prepore and pore particles were picked using the prepore and pore models in crYOLO (figs. S4, S6, and S12), and the percentage of pore state as a function of time was used to determine the rate of prepore-to-pore transition. In addition, we picked prepores and pores together using a general picking model in crYOLO and subjected the picked particles to 2D classification using ISAC (63) in SPHIRE (64). The numbers of particles in prepore and pore class averages were then quantified. To validate this quantification, we performed a Bayesian binomial regression following 2D classification to calculate the probability of obtaining pores using the mutant datasets as an example. The results mirrored the initial analysis (Fig. 6A and fig. S12D).

To test the influence of receptors on prepore-to-pore transition kinetics, 350.9 nM of either ABC WT or TcA WT (protomer concentration of TcA) was first mixed with its receptors. Then, the toxin-glycan mix was preincubated for 1 hour at 21°C in pH 7.5 buffer, before switching the pH to either pH 11.2 or pH 4 and incubating for a further 2 hours to induce prepore-to-pore transition. For this,

16.5× (5.8 μM) molar excess of the glycan receptors heparin and Lewis X (conjugated to BSA), as well as 70 nM Vsg (1:1 with the pentamer concentration of TcA), was used. Heparin, made from porcine intestinal mucosa, was procured from Merck (product number: 375054). BSA–Lewis X was prepared as previously described (12).

Subsequently, the samples were negatively stained, imaged, and quantified as previously described. For prepore-to-pore transition with heparin at pH 4, performing the experiment in buffer led to a severe aggregation of the protein (fig. S4B), presumably due to its strong negative charge, making quantification difficult. Therefore, to circumvent this, the experiment was performed directly on the negative stain grids. In this regard, the grids were first preincubated with 7 nM ABC WT (holotoxin) for 1 min before blotting and addition of the glycan. After a 30-min incubation of the grids with heparin in humid conditions, the buffer was exchanged to pH 4, and then they were incubated for another 2 hours before blotting, staining, and imaging. Quantified data were analyzed using an unpaired two-tailed *t* test. All experiments were performed with three technical replicates.

Cryo-EM sample and grid preparation

TcA (1279-At647N) contained all the mutations introduced in variants that were designed for labeling as previously described, namely, C16S, C20S, and C870S, as well as T1279C, the labeling site for the fluorophore At647N. Labeling was performed as previously described. TcA (K1179W) and ABC (K567W/K2008W) (holotoxin) were based on the unmodified TcA WT and therefore only included the aforementioned mutations: K1179W for TcA (K1179W) and K567W/K2008W for ABC (K567W/K2008W). For exposure to pH 11.2, TcA (0.25 mg/ml; 1279-At647N), TcA (0.9 mg/ml; K1179W), and ABC (0.5 mg/ml; K567W/K2008W), all in labeling buffer, were mixed with pH 11.2 buffer [100 mM CAPS-NaOH (pH 11.2), 150 mM NaCl, and 0.1% Tween 20] and incubated at 22°C for 6, 24, and 2 hours, respectively. Subsequently, the buffer was neutralized by mixing 1:1 with labeling buffer before 4 μl was loaded onto a freshly glow discharged Quantifoil 2/1 200 or 300 mesh gold grid with 2-nm amorphous carbon support. All samples were incubated on the grids for 5 min and then vitrified in liquid ethane using a Vitrobot Mark IV (Thermo Fisher Scientific) set to 100% humidity, 12°C, a blotting time of 3.0 s, and blot forces of −3 and 2 for TcA (1279-At647N) and ABC (K567W/K2008W), respectively. TcA (K1179W) was loaded on the grids in two rounds; in round 1, the sample was incubated for 5 min on the grid before blotting for 3.0 s, blot force of 1, and 0.5-s waiting time. Round 2 was the same as round one but without any waiting time.

Cryo-EM data acquisition

Cryo-EM datasets of TcA (1279-At647N) and ABC (K567W/K2008W) were collected with a Cs-corrected Titan Krios transmission electron microscope (Thermo Fisher Scientific) equipped with a X-FEG and a K3 direct electron detector with Bioquantum energy filter (Gatan) and a slit width of 15 eV. Images were recorded using the automated acquisition program EPU (Thermo Fisher Scientific) in a super-resolution mode at a magnification of 81,000, corresponding to a pixel size of 0.44 Å/pixel on the specimen level. Each movie comprised 60 frames acquired over a total integration time of 3.0 s with a total cumulative dose of ~78 and 57 e[−]/Å² for TcA (1279-At647N) and ABC (K567W/K2008W), respectively. A single dataset was collected for TcA (1279-At647N) with 13,059 movie-mode images acquired in a defocus

range of −1.2 to −3.0 μm. For ABC (K567W/K2008W), two datasets of 13,290 and 11,321 movies were acquired in a defocus range of −1.5 to −3.0 μm.

For TcA (K1179W), a single dataset was acquired with a Talos Arctica transmission electron microscope (Thermo Fisher Scientific) equipped with a X-FEG and a Falcon III direct electron detector operated in linear mode. Images were recorded using the automated acquisition program EPU (Thermo Fisher Scientific) at a magnification of 120,000, corresponding to a pixel size of 1.21 Å/pixel on the specimen level. Five thousand four hundred ninety-four movie-mode images were acquired in a defocus range of −1.5 to −2.75 μm. Each movie comprised 40 frames acquired over a total integration time of 3.0 s with a total cumulative dose of ~56 e[−]/Å².

Cryo-EM image processing

All movie frames were aligned, dose-corrected, binned twice to 0.88 Å/pixel in the case of TcA (1279-At647N) and ABC (K567W/K2008W) or left unbinned for TcA (K1179W), averaged using MotionCor2 (65), and contrast transfer function (CTF)-estimated using CTFIND4 (66), all implemented in TransPIRE (67). Particles were autopicked using crYOLO (62) with a general particle model and extracted with box sizes of 384, 352, and 560 pixels for TcA (1279-At647N), TcA (K1179W), and ABC (K567W/K2008W), respectively. Subsequently, reference-free 2D classification was performed using ISAC (63) in SPHIRE (64). Then, the “Beautifier” tool of SPHIRE (64) was applied to obtain refined and sharpened 2D class averages at the original pixel size, showing high-resolution features. 3D refinements were performed using MERIDIEN in SPHIRE (64) in C5 symmetry using the density map of TcdA1 WT [Electron Microscopy Data Bank (EMDB) ID 10033], low-pass-filtered to 20 Å, as the initial reference. This was followed by further processing in Relion 3.1 (68) including 3D refinement, particle polishing, as well as CTF and local refinements.

For TcA (K1179W), 390,444 particles were autopicked, and of those, 356,439 were subsequently extracted for 2D classification with a pixel size of 6.1 Å/pixel on the particle level. 2D classification resulted in 230,785 (99%) particle images corresponding to the prepore and 1921 (1%) particle images corresponding to the pore state of TcA (fig. S14, A and B). After initial 3D refinement, the particles were centered and reextracted using the rotation/translation parameters obtained in MERIDIEN, and 3D refinement was repeated using a mask that included the well-resolved part of the reconstruction. Furthermore, processing was performed in Relion 3.1 (68) resulting in a final average resolution of 2.9 Å according to FSC 0.143 (fig. S14C), which was used for model building. This density map showed a prepore-to-pore intermediate state lacking densities corresponding to RBDs B and C (fig. S14, D and E). Lowering the binarization threshold revealed an additional density below RBD D, next to the neuraminidase-like domain (fig. S14F). A 3D classification performed with a mask focused on this density resulted in three classes of 160,851, 21,440, and 48,494 particles respectively. 3D refinement of the largest class produced a 3.3-Å map according to FSC 0.143 that showed the same elongated extra density below RBD D at a low binarization threshold (fig. S14F).

For TcA (1279-At647N), 573,814 particles were autopicked and used for a reference-free 2D classification with a pixel size of 4.40 Å/pixel on the particle level followed by Beautifier to obtain 2D class averages showing high-resolution features (fig. S15, A and B). 2D

classification resulted in 80,710 (35%) particle images corresponding to the prepore and 150,465 (65%) particle images corresponding to the pore state of TcA. After the initial 3D refinement, the particles were centered, reextracted, and refined as previously described resulting in a prepore-to-pore intermediate map with an average resolution of 3.8 Å according to FSC 0.143. Then, an additional CTF refinement, followed by 3D refinement in Relion 3.1 (68), yielded a reconstruction with a final average resolution of 3.6 Å according to FSC 0.143 (fig. S15, C to F), which was used for model building. 3D variance analysis of this latter reconstruction also revealed an additional slightly elongated density at the lower part of the shell. To improve this density, we applied 3D classification using Sort3D_DEPTH in SPHIRE with a mask focusing on the bottom of TcA (fig. S15F). We obtained three 3D classes with 21,332, 20,992, and 16,447 particles, respectively. The largest 3D class showed an elongated additional density below RBD D, next to the neuraminidase-like domain as previously observed. Furthermore, local refinement of this 3D class with 1.875° initial angular sampling and subsequent postprocessing with the PostRefiner tool improved this extra density, which became visible at the low binarization threshold of the resulting map of 4.2 Å according to FSC 0.143 (fig. S15F).

The two ABC (K567W/K2008W) datasets yielded 426,857 and 509,274 particles, respectively, which were classified in 2D, with a pixel size of 6.1 Å/pixel on the particle level, and 3D-refined. Subsequently, the particles were centered, reextracted, and combined, yielding a total of 61,817 (61%) and 29,942 (39%) prepore and pore particles of TcA, respectively, after a final round of 2D classification (fig. S16, A and B). The prepore particles were further processed iteratively with 2D classifications combined with 3D refinements to obtain centered, high-quality holotoxin classes. Ultimately, 13,356 particles were taken for 3D refinement with Relion 3.1 (68) resulting in a reconstruction with an average resolution of 3.3 Å according to FSC 0.143 (fig. S16, C to E). As observed previously with TcA (1279-At647N) and TcA (K1179W), the obtained reconstruction lacked density corresponding to the RBDs B and C but showed an additional density below RBD D at the low binarization threshold. Subsequent 3D classification in Relion 3.1 with a mask focusing on the additional density (fig. S16F) resulted in relatively homogeneous 3D classes which could be taken for additional CTF and local refinement. Since the presence of the TcB-TcC cocoon did not show any effect on prepore-to-pore kinetics (fig. S2, C and F), the final post-processing step of ABC (K567W/K2008W) was performed with a mask on the TcA pentamer only to yield a 3.2-Å map according to FSC 0.143 (fig. S16F), which was used for model building.

Atomic model building and refinement

For TcA (1279-At647N), we first rigid-body fitted the model of the TcA-WT prepore (PDB 6RW6) into the obtained density map of the intermediate using UCSF Chimera (69) and truncated residues 21 to 93 (N terminus) and 1309 to 1580 (RBDs B and C), for which no density was present. At the region corresponding to RBD A (residues 298 to 432), the reconstruction showed a density turned outward away from the main density at an angle of 20°. To determine whether this density belonged to RBD A, we first predicted the model of RBD A using the protein prediction software AlphaFold 2 (70). Subsequently, the resultant best model was rigid-body fitted into the density of the cryo-EM map and joined with the rest of the model after manual adjustment in Coot (71). Then, the combined model was refined using ISOLDE (72), followed by the real space refinement tool of PHENIX (73).

Next, since the observed extra density lacked high-resolution features that would allow tight fitting and model building, we performed map subtraction of the best 3D class of TcA (1279-At647N) showing this density from the global EM density map to obtain the difference map of the elongated density. Then, we low-pass-filtered this difference map to 10 Å and aligned it to the reconstruction and fitted the model of TcA (1279-At647N). This elongated density fit to the space below the region corresponding to RBD B suggesting the RBD B (and perhaps also RBD C) was flipped out. Therefore, we rigid-body fitted residues 1309 to 1361 and 1493 to 1576 corresponding to RBD B into the additional density of all the maps of the TcA intermediate state but could not fit RBD C due to insufficient density. The difference map showing the additional density corresponding to RBD B was not included in the density maps submitted to EMDB.

Atomic models of ABC (K567W/K2008W) and TcA (K1179W) were built on the basis of the TcA (1279-At647N) model following the same procedure. Briefly, the model of TcA (1279-At647N) was first rigid-body fitted into the obtained density maps of the prepore-to-pore intermediates using UCSF Chimera (69). Here, the relevant mutations were added, before the models were manually adjusted in Coot and subsequently refined in ISOLDE and PHENIX. The data statistics of all obtained models are summarized in table S6.

Supplementary Materials

The PDF file includes:

Figs. S1 to S23
Legends for movies S1 and S2
Tables S1 to S11
Supplementary Notes
Supplementary Methods
Legend for source data
References

Other Supplementary Material for this manuscript includes the following:

Movies S1 and S2
Source Data

REFERENCES AND NOTES

1. D. Roderer, S. Raunser, Tc toxin complexes: Assembly, membrane permeation, and protein translocation. *Annu. Rev. Microbiol.* **73**, 247–265 (2019).
2. N. R. Waterfield, D. J. Bowen, J. D. Fetherston, R. D. Perry, R. H. Ffrench-Constant, The tc genes of *Photobacterium*: A growing family. *Trends Microbiol.* **9**, 185–191 (2001).
3. R. Ffrench-Constant, N. Waterfield, An ABC guide to the bacterial toxin complexes. *Adv. Appl. Microbiol.* **58**, 169–183 (2005).
4. D. Bowen, T. a. Rocheleau, M. Blackburn, O. Andreev, E. Golubeva, R. Bhartia, R. H. Ffrench-Constant, Insecticidal toxins from the bacterium *Photobacterium luminescens*. *Science* **280**, 2129–2132 (1998).
5. E. E. Herbert, H. Goodrich-Blair, Friend and foe: The two faces of *Xenorhabdus nematophila*. *Nat. Rev. Microbiol.* **5**, 634–646 (2007).
6. T. D. Hey, A. D. Schleper, S. A. Bevan, S. B. Bintrim, J. C. Mitchell, Z. S. Li, W. Ni, B. Zhu, D. J. Merlo, P. C. Apel-birkhold, T. Meade, Mixing and matching TC proteins for pest control, US Patent US 7,491,698 B2 (2009), 1–222.
7. N. Waterfield, M. Hares, S. Hinchliffe, B. Wren, R. Ffrench-Constant, "The insect toxin complex of *Yersinia*" in *The Genus Yersinia. Advances in Experimental Medicine and Biology*, Perry, R. D. Fetherston, J. D., Eds. (Springer, 2007), vol. 603, pp. 247–257.
8. S. M. Tennant, N. a. Skinner, A. Joe, R. M. Robins-Browne, Homologues of insecticidal toxin complex genes in *Yersinia enterocolitica* biotype 1A and their contribution to virulence. *Infect. Immun.* **73**, 6860–7 (2005).
9. D. Bowen, J. Ensign, Purification and characterization of a high-molecular-weight insecticidal protein complex produced by the entomopathogenic bacterium *Photobacterium luminescens*. *Appl. Environ. Microbiol.* **64**, 3029–35 (1998).
10. M. J. Landsberg, S. a. Jones, R. Rothnagel, J. N. Busby, S. D. G. Marshall, R. M. Simpson, J. S. Lott, B. Hankamer, M. R. H. Hurst, 3D structure of the *Yersinia entomophaga* toxin complex and implications for insecticidal activity. *Proc. Natl. Acad. Sci. U.S.A.* **108**, 20544–9 (2011).

11. D. Roderer, E. Schubert, O. Sitsel, S. Raunser, Towards the application of Tc toxins as a universal protein translocation system. *Nat. Commun.* **10**, 5263 (2019).
12. D. Roderer, F. Bröcker, O. Sitsel, P. Kaplonek, F. Leidreiter, P. H. Seeberger, S. Raunser, Glycan-dependent cell adhesion mechanism of Tc toxins. *Nat. Commun.* **11**, 2694 (2020).
13. C. Gatsogiannis, A. E. Lang, D. Meusch, V. Pfaumann, O. Hofnagel, R. Benz, K. Aktories, S. Raunser, A syringe-like injection mechanism in *Photobacterium luminescens* toxins. *Nature* **495**, 520–523 (2013).
14. F. Leidreiter, D. Roderer, D. Meusch, C. Gatsogiannis, R. Benz, S. Raunser, Common architecture of Tc toxins from human and insect pathogenic bacteria. *Sci. Adv.* **5**, eaax6497 (2019).
15. N. Song, L. Chen, X. Ren, N. R. Waterfield, J. Yang, G. Yang, N-glycans and sulfated glycosaminoglycans contribute to the action of diverse Tc toxins on mammalian cells. *PLoS Pathog.* **17**, e1009244 (2021).
16. S. J. Piper, L. Brillault, R. Rothnagel, T. I. Croll, J. K. Box, I. Chassagnon, S. Scherer, K. N. Goldie, S. A. Jones, F. Schepers, L. Hartley-Tassell, T. Ve, J. N. Busby, J. E. Dalziel, J. S. Lott, B. Hankamer, H. Stahlberg, M. R. H. Hurst, M. J. Landsberg, Cryo-EM structures of the pore-forming A subunit from the *Yersinia entomophaga* ABC toxin. *Nat. Commun.* **10**, 1952 (2019).
17. P. N. Ng'ang'a, L. Siukstaite, A. E. Lang, H. Bakker, W. Römer, K. Aktories, G. Schmidt, Involvement of N-glycans in binding of *Photobacterium luminescens* Tc toxin. *Cell Microbiol.* **23**, e13326 (2021).
18. Y. Xu, R. Viswanatha, O. Sitsel, D. Roderer, H. Zhao, C. Ashwood, C. Voelcker, S. Tian, S. Raunser, N. Perrimon, M. Dong, CRISPR screens in *Drosophila* cells identify Vsg as a Tc toxin receptor. *Nature* **610**, 349–355 (2022).
19. D. Meusch, C. Gatsogiannis, R. G. Efremov, A. E. Lang, O. Hofnagel, I. R. Vetter, K. Aktories, S. Raunser, Supplementary: Mechanism of Tc toxin action revealed in molecular detail. *Nature* **508**, 61–65 (2014).
20. J. N. Busby, S. Panjikar, M. J. Landsberg, M. R. H. Hurst, J. S. Lott, The BC component of ABC toxins is an RHS-repeat-containing protein encapsulation device. *Nature* **501**, 547–550 (2013).
21. S. Dong, W. Zheng, N. Pinkerton, J. Hansen, S. B. Tikunova, J. P. Davis, S. M. Heissler, E. Kudryashova, E. H. Egelman, D. S. Kudryashov, *Photobacterium luminescens* Tccc3 toxin targets the dynamic population of F-actin and impairs cell cortex integrity. *Int. J. Mol. Sci.* **23**, 7026 (2022).
22. A. Belyy, F. Lindemann, D. Roderer, J. Funk, B. Bardiaux, J. Protze, P. Bieling, H. Oschkinat, S. Raunser, Mechanism of threonine ADP-ribosylation of F-actin by a Tc toxin. *Nat. Commun.* **13**, 4202 (2022).
23. A. E. Lang, G. Schmidt, A. Schlosser, T. D. Hey, I. M. Larrinua, J. J. Sheets, H. G. Mannherz, K. Aktories, *Photobacterium luminescens* toxins ADP-ribosylate actin and RhoA to force actin clustering. *Science* **327**, 1139–1142 (2010).
24. C. Gatsogiannis, F. Merino, D. Roderer, D. Balchin, E. Schubert, A. Kuhlee, M. Hayer-Hartl, S. Raunser, Tc toxin activation requires unfolding and refolding of a β -propeller. *Nature* **563**, 209–213 (2018).
25. C. Gatsogiannis, F. Merino, D. Prumbaum, D. Roderer, F. Leidreiter, D. Meusch, S. Raunser, Membrane insertion of a Tc toxin in near-atomic detail. *Nat. Struct. Mol. Biol.* **23**, 884–890 (2016).
26. D. Roderer, O. Hofnagel, R. Benz, S. Raunser, Structure of a Tc holotoxin pore provides insights into the translocation mechanism. *Proc. Natl. Acad. Sci. U.S.A.* **116**, 23083–23090 (2019).
27. P. N. Ng'ang'a, J. K. Ebner, M. Plessner, K. Aktories, G. Schmidt, P. N. Ng'ang'a, J. K. Ebner, M. Plessner, K. Aktories, G. Schmidt, Engineering *Photobacterium luminescens* toxin complex (PTC) into a recombinant injection nanomachine. *Life Sci. Alliance* **2**, e201900485 (2019).
28. J. A. T. Dow, Extremely high pH in biological systems: A model for carbonate transport. *Am. J. Physiol. Regul. Integr. Comp. Physiol.* **246**, R633–R636 (1984).
29. G. S. Ost, P. N. Ng'ang'a, A. E. Lang, K. Aktories, *Photobacterium luminescens* Tc toxin is inhibited by the protease inhibitor MG132 and activated by protease cleavage resulting in increased binding to target cells. *Cell Microbiol.* **21**, e12978 (2019).
30. H. Frauenfelder, F. Parak, R. D. Young, Conformational substates in proteins. *Annu. Rev. Biophys. Chem.* **17**, 451–479 (1988).
31. F. Rico, A. Russek, L. González, H. Grubmüller, S. Scheuring, Heterogeneous and rate-dependent streptavidin–biotin unbinding revealed by high-speed force spectroscopy and atomistic simulations. *Proc. Natl. Acad. Sci. U.S.A.* **116**, 6594–6601 (2019).
32. C. Möckel, J. Kubiak, O. Schillinger, R. Kühnemuth, D. Della Corte, G. F. Schröder, D. Willbold, B. Strodel, C. A. M. Seidel, P. Neudecker, Integrated NMR, fluorescence, and molecular dynamics benchmark study of protein mechanics and hydrodynamics. *J. Phys. Chem. B* **123**, 1453–1480 (2019).
33. L. Edman, Z. Földes-Papp, S. Wennmalm, R. Rigler, The fluctuating enzyme: A single molecule approach. *Chem. Phys.* **247**, 11–22 (1999).
34. S. Stoll, A. Schweiger, EasySpin, a comprehensive software package for spectral simulation and analysis in EPR. *J. Magn. Reson.* **178**, 42–55 (2006).
35. R. Anandakrishnan, B. Aguilar, A. V. Onufriev, H++ 3.0: Automating pK prediction and the preparation of biomolecular structures for atomistic molecular modeling and simulations. *Nucleic Acids Res.* **40**, W537–41 (2012).
36. O. Smithies, Disulfide-bond cleavage and formation in proteins. *Science* **150**, 1595–1598 (1965).
37. P. Knight, Hydrolysis of p-NN'-phenylenebismaleimide and its adducts with cysteine. Implications for cross-linking of proteins. *Biochem. J.* **179**, 191–197 (1979).
38. S. Bleicken, T. E. Assafa, H. Zhang, C. Elsner, I. Ritsch, M. Pink, S. Rajca, G. Jeschke, A. Rajca, E. Bordignon, gem-Diethyl pyrroline nitroxide spin labels: Synthesis, EPR characterization, rotamer libraries and biocompatibility. *ChemistryOpen* **8**, 1057–1065 (2019).
39. G. Jeschke, MMM: A toolbox for integrative structure modeling. *Protein Sci.* **27**, 76–85 (2018).
40. Y. Polyhach, E. Bordignon, G. Jeschke, Rotamer libraries of spin labelled cysteines for protein studies. *Phys. Chem. Chem. Phys.* **13**, 2356–2366 (2011).
41. R. Tschaggelar, B. Kasumaj, M. G. Santangelo, J. Forrer, P. Leger, H. Dube, F. Diederich, J. Harmer, R. Schuhmann, I. García-Rubio, G. Jeschke, Cryogenic 35 GHz pulse ENDOR probehead accommodating large sample sizes: Performance and applications. *J. Magn. Reson.* **200**, 81–87 (2009).
42. Y. Polyhach, E. Bordignon, R. Tschaggelar, S. Gandra, A. Godt, G. Jeschke, High sensitivity and versatility of the DEER experiment on nitroxide radical pairs at Q-band frequencies. *Phys. Chem. Chem. Phys.* **14**, 10762–10773 (2012).
43. M. Pannier, S. Veit, A. Godt, G. Jeschke, H. W. Spiess, Dead-time free measurement of dipole–dipole interactions between electron spins. *J. Magn. Reson.* **142**, 331–340 (2000).
44. C. E. Tait, S. Stoll, Coherent pump pulses in double electron electron resonance spectroscopy. *Phys. Chem. Chem. Phys.* **18**, 18470–18485 (2016).
45. M. Teucher, E. Bordignon, Improved signal fidelity in 4-pulse DEER with Gaussian pulses. *J. Magn. Reson.* **296**, 103–111 (2018).
46. S. G. Worswick, J. A. Spencer, G. Jeschke, I. Kuprov, Deep neural network processing of DEER data. *Sci. Adv.* **4**, 1–18 (2018).
47. G. Jeschke, V. Chechik, P. Ionita, A. Godt, H. Zimmermann, J. Banham, C. R. Timmel, D. Hilger, H. Jung, DeerAnalysis2006—A comprehensive software package for analyzing pulsed ELDOR data. *Appl. Magn. Reson.* **30**, 473–498 (2006).
48. O. Schiemann, C. A. Heubach, D. Abdullin, K. Ackermann, M. Azarkh, E. G. Bagryanskaya, M. Drescher, B. Endeward, J. H. Freed, L. Galazzo, D. Goldfarb, T. Hett, L. Esteban Hofer, L. Fábregas Ibáñez, E. J. Hustedt, S. Kucher, I. Kuprov, J. E. Lovett, A. Meyer, S. Ruthstein, S. Saxena, S. Stoll, C. R. Timmel, M. Di Valentin, H. S. Mchaourab, T. F. Prisner, B. E. Bode, E. Bordignon, M. Bennati, G. Jeschke, Benchmark test and guidelines for DEER/PELDOR experiments on nitroxide-labeled biomolecules. *J. Am. Chem. Soc.* **143**, 17875–17890 (2021).
49. T. Von Hagens, Y. Polyhach, M. Sajid, A. Godt, G. Jeschke, Suppression of ghost distances in multiple-spin double electron–electron resonance. *Phys. Chem. Chem. Phys.* **15**, 5854–5866 (2013).
50. J. Widengren, V. Kudryavtsev, M. Antonik, S. Berger, M. Gerken, C. A. M. Seidel, Single-molecule detection and identification of multiple species by multiparameter fluorescence detection. *Anal. Chem.* **78**, 2039–2050 (2006).
51. V. Kudryavtsev, M. Sikor, S. Kalinin, D. Mokranjac, C. A. M. Seidel, D. C. Lamb, Combining MFD and PIE for accurate single-pair Förster resonance energy transfer measurements. *ChemPhysChem* **13**, 1060–1078 (2012).
52. S. Kalinin, T. Peulen, S. Sindbert, P. J. Rothwell, S. Berger, T. Restle, R. S. Goody, H. Gohlke, C. A. M. Seidel, A toolkit and benchmark study for FRET-restrained high-precision structural modeling. *Nat. Methods* **9**, 1218–1225 (2012).
53. J. R. Fries, L. Brand, C. Eggeling, M. Köllner, C. A. M. Seidel, Quantitative identification of different single molecules by selective time-resolved confocal fluorescence spectroscopy. *J. Phys. Chem. A* **102**, 6601–6613 (1998).
54. S. Kalinin, A. Valeri, M. Antonik, S. Felekyan, C. A. M. Seidel, Detection of structural dynamics by FRET: A photon distribution and fluorescence lifetime analysis of systems with multiple states. *J. Phys. Chem. B* **114**, 7983–7995 (2010).
55. S. Kalinin, S. Felekyan, M. Antonik, C. A. M. Seidel, Probability distribution analysis of single-molecule fluorescence anisotropy and resonance energy transfer. *J. Phys. Chem. B* **111**, 10253–10262 (2007).
56. S. Preus, S. L. Noer, L. L. Hildebrandt, D. Gudnason, V. Birkedal, iSMS: Single-molecule FRET microscopy software. *Nat. Methods* **12**, 593–594 (2015).
57. V. Devaugs, C. Marquer, S. Lécart, J.-C. Cossec, M.-C. Potier, E. Fort, K. Suhling, S. Lévêque-Fort, Homodimerization of amyloid precursor protein at the plasma membrane: A homoFRET study by time-resolved fluorescence anisotropy imaging. *PLoS ONE* **7**, e44434 (2012).
58. F. Ströhl, H. H. W. Wong, C. E. Holt, C. F. Kaminski, Total internal reflection fluorescence anisotropy imaging microscopy: Setup, calibration, and data processing for protein polymerization measurements in living cells. *Methods Appl. Fluoresc.* **6**, 014004 (2018).
59. M. Dimura, T.-O. Peulen, H. Sanabria, D. Rodnin, K. Hemmen, C. A. Hanke, C. A. M. Seidel, H. Gohlke, Automated and optimally FRET-assisted structural modeling. *Nat. Commun.* **11**, 5394 (2020).

60. T. O. Peulen, O. Opanasyuk, C. A. M. Seidel, Combining graphical and analytical methods with molecular simulations to analyze time-resolved FRET measurements of labeled macromolecules accurately. *J. Phys. Chem. B* **121**, 8211–8241 (2017).
61. J. Schindelin, I. Arganda-Carreras, E. Frise, V. Kaynig, M. Longair, T. Pietzsch, S. Preibisch, C. Rueden, S. Saalfeld, B. Schmid, J. Y. Tinevez, D. J. White, V. Hartenstein, K. Eliceiri, P. Tomancak, A. Cardona, Fiji: An open-source platform for biological-image analysis. *Nat. Methods* **9**, 676–682 (2012).
62. T. Wagner, F. Merino, M. Stabrin, T. Moriya, C. Antoni, A. Apelbaum, P. Hagel, O. Sitsel, T. Raisch, D. Prumbaum, D. Quentin, D. Roderer, S. Tacke, B. Siebolds, E. Schubert, T. R. Shaikh, P. Lill, C. Gatsogiannis, S. Raunser, SPHIRE-crYOLO is a fast and accurate fully automated particle picker for cryo-EM. *Commun. Biol.* **2**, 1–13 (2019).
63. Z. Yang, J. Fang, J. Chittuluru, F. J. Asturias, P. A. Penczek, Iterative stable alignment and clustering of 2D transmission electron microscope images. *Structure* **20**, 237–247 (2012).
64. T. Moriya, M. Saur, M. Stabrin, F. Merino, H. Voicu, Z. Huang, P. A. Penczek, S. Raunser, C. Gatsogiannis, High-resolution single particle analysis from electron cryo-microscopy images using SPHIRE. *J. Vis. Exp.* **123**, 55448 (2017).
65. S. Q. Zheng, E. Palovcak, J. P. Armache, K. A. Verba, Y. Cheng, D. A. Agard, MotionCor2: Anisotropic correction of beam-induced motion for improved cryo-electron microscopy. *Nat. Methods* **14**, 331–332 (2017).
66. A. Rohou, N. Grigorieff, CTFFIND4: Fast and accurate defocus estimation from electron micrographs. *J. Struct. Biol.* **192**, 216–221 (2015).
67. M. Stabrin, F. Schoenfeld, T. Wagner, S. Pospich, C. Gatsogiannis, S. Raunser, TranSPHIRE: Automated and feedback-optimized on-the-fly processing for cryo-EM. *Nat. Commun.* **11**, 1–14 (2020).
68. S. H. W. Scheres, RELION: Implementation of a Bayesian approach to cryo-EM structure determination. *J. Struct. Biol.* **180**, 519–530 (2012).
69. E. F. Pettersen, T. D. Goddard, C. C. Huang, G. S. Couch, D. M. Greenblatt, E. C. Meng, T. E. Ferrin, UCSF Chimera—A visualization system for exploratory research and analysis. *J. Comput. Chem.* **25**, 1605–1612 (2004).
70. J. Jumper, R. Evans, A. Pritzel, T. Green, M. Figurnov, O. Ronneberger, K. Tunyasuvunakool, R. Bates, A. Žídek, A. Potapenko, A. Bridgland, C. Meyer, S. A. A. Kohl, A. J. Ballard, A. Cowie, B. Romera-Paredes, S. Nikolov, R. Jain, J. Adler, T. Back, S. Petersen, D. Reiman, E. Clancy, M. Zielinski, M. Steinegger, M. Pacholska, T. Berghammer, S. Bodenstein, D. Silver, O. Vinyals, A. W. Senior, K. Kavukcuoglu, P. Kohli, D. Hassabis, Highly accurate protein structure prediction with AlphaFold. *Nature* **596**, 583–589 (2021).
71. P. Emsley, B. Lohkamp, W. G. Scott, K. Cowtan, Features and development of Coot. *Acta Crystallogr. D. Biol. Crystallogr.* **66**, 486–501 (2010).
72. T. I. Croll, ISOLDE: A physically realistic environment for model building into low-resolution electron-density maps. *Acta Crystallogr. D. Struct. Biol.* **74**, 519–530 (2018).
73. P. V. Afonine, B. P. Klaholz, N. W. Moriarty, B. K. Poon, O. V. Sobolev, T. C. Terwilliger, P. D. Adams, A. Urzhumtsev, New tools for the analysis and validation of cryo-EM maps and atomic models. *Acta Crystallogr. D. Struct. Biol.* **74**, 814–840 (2018).
74. B. Hellenkamp, S. Schmid, O. Doroshenko, O. Opanasyuk, R. Kühnemuth, S. Rezaei Adariani, B. Ambrose, M. Aznauryan, A. Barth, V. Birkedal, M. E. Bowen, H. Chen, T. Cordes, T. Eilert, C. Fijen, C. Gebhardt, M. Götz, G. Gouridis, E. Gratton, T. Ha, P. Hao, C. A. Hanke, A. Hartmann, J. Hendrix, L. L. Hildebrandt, V. Hirschfeld, J. Hohlbein, B. Hua, C. G. Hübner, E. Kallis, A. N. Kapanidis, J. Y. Kim, G. Krainer, D. C. Lamb, N. K. Lee, E. A. Lemke, B. Levesque, M. Levitus, J. J. McCann, N. Naredi-Rainer, D. Nettels, T. Ngo, R. Qiu, N. C. Robb, C. Röcker, H. Sanabria, M. Schlierf, T. Schröder, B. Schuler, H. Seidel, L. Streit, J. Thurn, P. Tinnefeld, S. Tyagi, N. Vandenberk, A. M. Vera, K. R. Weninger, B. Wünsch, I. S. Yanez-Orozco, J. Michaelis, C. A. M. Seidel, T. D. Craggs, T. Hugel, Precision and accuracy of single-molecule FRET measurements—A multi-laboratory benchmark study. *Nat. Methods* **15**, 669–676 (2018).
75. T. E. Tomov, R. Tsukanov, R. Masoud, M. Liber, N. Plavner, E. Nir, Disentangling subpopulations in single-molecule FRET and ALEX experiments with photon distribution analysis. *Biophys. J.* **102**, 1163–1173 (2012).
76. S. Sindbert, S. Kalinin, H. Nguyen, A. Kienzler, L. Clima, W. Bannwarth, B. Appel, S. Müller, C. A. M. Seidel, Accurate distance determination of nucleic acids via Förster resonance energy transfer: Implications of dye linker length and rigidity. *J. Am. Chem. Soc.* **133**, 2463–2480 (2011).
77. M. Antonik, S. Felekyan, A. Gaiduk, C. A. M. Seidel, Separating structural heterogeneities from stochastic variations in fluorescence resonance energy transfer distributions via photon distribution analysis. *J. Phys. Chem. B* **110**, 6970–6978 (2006).
78. D. Axelrod, Selective imaging of surface fluorescence with very high aperture microscope objectives. *J. Biomed. Opt.* **6**, 6–13 (2001).

Acknowledgments: We thank K. Vogel-Bachmayr, O. Hofnagel, and T. Wagner for technical support in the wet lab, EM facility, and statistical analysis, respectively. We thank H. Grubmüller for stimulating discussions. **Funding:** This work was supported by funds from the Max Planck Society (to S.R.) and the European Research Council under the European Union's Horizon 2020 Programme (ERC-2019-SyG, grant no. 856118 to S.R.), by the Deutsche Forschungsgemeinschaft (DFG, German Research Foundation) under Germany's Excellence Strategy—EXC 2033–390677874—RESOLV (to E.B.), by funds from the University of Geneva (to E.B.) and Heinrich Heine University (to C.A.M.S.), and by the European Research Council under the European Union's Horizon Programme (ERC-2014-AdG, hybridFRET grant no. 671208 to C.A.M.S.). J.F. acknowledges the support of the International Helmholtz Research School of Biophysics and Soft Matter (BioSoft). **Author contributions:** Conceptualization: S.R., E.B., and C.A.M.S. Supervision: S.R., E.B. and C.A.M.S. Writing—original draft: P.N.N., E.B., C.A.M.S., and S.R. Writing—review and editing: P.N.N., T.E.A., S.K., E.B., J.F., D.R., C.A.M.S., O.S., A.B., D.P., and S.R. Methodology: E.B., R.K., T.E.A., P.N.N., O.S., S.K., J.F., and C.A.M.S. Investigation: D.R., R.K., P.N.N., O.S., A.B., S.K., T.E.A., and J.F. Validation: S.R., E.B., P.N.N., R.K., S.K., C.A.M.S., and J.F. Formal analysis: E.B., D.R., D.P., R.K., P.N.N., A.B., S.K., C.A.M.S., and J.F. Visualization: D.R., R.K., P.N.N., A.B., S.K., J.F., and C.A.M.S. Data curation: R.K. and J.F. Resources: Y.X., M.D., J.F., C.A.M.S., and S.R. Funding acquisition: S.R., E.B., and C.A.M.S. Project administration: S.R., E.B., R.K., and C.A.M.S. **Competing interests:** The authors declare that they have no competing interests. **Data and materials availability:** The cryo-EM densities of TcA (1279-At647N), TcA (K1179W), and TcA (K567W/K2008W) have been deposited to the EMDB under accession codes EMD-16793, EMD-16791, and EMD-16792, respectively. These depositions include sharpened maps, unfiltered half-maps, and the refinement masks. The atomic coordinates of the protein structures have been submitted to the PDB under accession codes 8CQ2, 8CPZ, and 8CQ0, respectively. All data needed to evaluate the conclusions in the paper are present in the paper and/or the Supplementary Materials. Source data are provided with this paper.

Submitted 20 June 2024
Accepted 12 November 2024
Published 3 January 2025
10.1126/sciadv.adr2019